Investigating the basal shear zone of the submarine Tuaheni Landslide Complex, New Zealand: a core-log-seismic integration study

Crutchley, G.J.[1*], Elger, J.[1], Kuhlmann, J.[2], Mountjoy, J.J.[3], Orpin, A.[3], Georgiopoulou, A.[4], Carey, J.[5], Dugan, B.[6], Cardona, S.[6], Han, S.[7], Cook, A.[8], Screaton, E.J.[9], Pecher, I.A.[10], Barnes, P.[3], Huhn, K.[2]

1. *GEOMAR Helmholtz Centre for Ocean Research Kiel, Germany*
2. *Centre for Marine Environmental Sciences (MARUM), University of Bremen, Germany*
3. *National Institute of Water and Atmospheric Research (NIWA), Wellington, New Zealand*
4. *School of Environment and Technology, University of Brighton, United Kingdom*
5. *GNS Science, Lower Hutt, New Zealand*
6. *Colorado School of Mines, U.S.A.*
7. *Jackson School of Geosciences, The University of Texas at Austin, U.S.A.*
8. *Ohio State University, U.S.A.*
9. *University of Florida, U.S.A.*
10. *School of Environment, University of Auckland, New Zealand*

*Corresponding author email address: gcrutchley@geomar.de

Key Points

We integrate scientific drilling data with seismic reflection data to investigate the submarine Tuaheni Landslide Complex

Basal shear zone of the landslide likely exploited a relatively low shear strength interval within an older (buried) mass transport deposit

Landslide emplacement seems to have induced an additional weak zone that is shallower than the interpreted base of the landslide deposit

Abstract

Although submarine landslides have been studied for decades, a persistent challenge is the integration of diverse geoscientific datasets to characterise failure processes. We present a core-log-seismic integration study of the Tuaheni Landslide Complex to investigate intact sediments beneath the undeformed seafloor as well as post-failure landslide deposits. Beneath the undeformed seafloor are coherent reflections underlain by a weakly-reflective and chaotic seismic unit. This chaotic unit is characterised by variable shear strength that correlates with density fluctuations. The basal shear zone of the Tuaheni landslide likely exploited one (or more) of the low shear strength intervals. Within landslide deposits is a widespread "Intra-debris Reflector", previously interpreted as the landslide's basal shear zone. This reflector is a subtle impedance drop around the boundary between upper and lower landslide units. However, there is no pronounced shear strength change across this horizon. Rather, there is a pronounced reduction in shear strength ~10-15 m above the Intra-debris Reflector that presumably represents an induced weak layer that developed during failure. Free gas accumulates beneath some regions of the landslide and is widespread deeper in the sedimentary sequence, suggesting that free gas may have played a role in pre-conditioning the slope to failure. Additional pre-conditioning or failure triggers could have been seismic shaking and associated transient fluid pressure. Our study underscores the importance of detailed core-log-seismic integration approaches for investigating basal shear zone development in submarine landslides.

Plain Language Summary

Submarine landslides move enormous amounts of sediment across the seafloor, and have the potential to generate damaging tsunamis. To understand how submarine landslides develop, we need to be able to *image* and *sample* beneath the seafloor in regions where landslides have occurred. To image beneath the seafloor we generate sound waves in the ocean and record reflections from those waves, enabling us to produce "seismic images" of sediment layers and structures beneath the seafloor. We then use scientific drilling to sample the sediment layers and measure physical properties. In this study, we combine seismic images and drilling results to investigate a submarine landslide east of New Zealand's North Island. Drilling next to the landslide revealed a ~25 m-thick layer of sediment (from ~75-95 metres below the seafloor) that has strong variations in sediment strength and density. We infer that intervals of relatively low strength within this layer developed into the main sliding surface of the landslide. Additionally, results from within the landslide suggest that the process of landslide emplacement has induced a zone of weak sediments closer to the seafloor. Our study demonstrates how combining seismic images and drilling data helps to understand submarine landslide processes.

Keywords

1. Introduction

Submarine landslides span a broad range of scales on Earth's active and passive continental margins and can incorporate volumes of sediment far in excess of terrestrial landslides (Hampton et al., 1996; Urlaub et al., 2013). A general feature of submarine landslides is that they often occur on very gentle slope gradients of less than 2°, and elevated pore fluid pressures are interpreted as a critical component for destabilising the slopes (e.g. Masson et al. 2006, 2010; Talling et al., 2014). The most commonly cited process for generating excess fluid pressure in the sub-seafloor is rapid accumulation of low-permeability sediment (Gibson, 1958; Dugan and Flemings, 2000). Another possible origin for excess pore pressure comes from gas hydrate systems; a causative link between gas hydrates and the triggering of submarine landslides was first proposed in the 1970s (McIver, 1977). Since then, the potential role of gas hydrates/free gas in slope destabilisation has received much research attention (e.g. Bünz et al., 2003; Field and Barber, 1993; Paull et al., 1996; Sultan et al., 2004; Mountjoy et al. 2014; Elger et al. 2018). Despite decades of research into this apparent association, there is still no clear evidence that gas hydrates play a significant role in destabilising sediments to the point of slope failure.

In addition to excess pore pressure, there are a several other factors that can either trigger or contribute to submarine landslide initiation and progressive failure. These include earthquakes, such as the 1929 Grand Banks submarine landslide (Piper et al. 1999), and the existence of weak layers within the stratigraphy (e.g. Masson et al. 2006; 2010; L'Heureux et al. 2011). Weak layers can generally be grouped into two main classes: inherited and induced weak layers (Locat et al. 2014). Inherited weak layers are distinct layers where the shear strength is lower than that of surrounding layers, prior to destabilization of the slope. Induced weak layers, by contrast, are developed during the process of sliding, for example through the process of strain softening (Kvalstad et al. 2005a). Inherited weak layers can be the result of weak lithologies (e.g. L'Heureux et al. 2011; Miramontes et al. 2018; Urlaub et al. 2018), but also through localised accumulation of excess pore fluid pressure (Locat et al. 2011; 2014; Dugan and Flemings, 2000). In many cases, the roles of lithology, differential consolidation and pore pressure accumulation are likely to be interwoven (e.g. Stegmann et al. 2007; Dugan and Flemings, 2000; Flemings et al. 2002; Urlaub et al. 2018).

In this study, we combine three-dimensional (3D) seismic data with logging-while-drilling (LWD) data, sediment core physical property measurements and line-scans, to investigate the Tuaheni Landslide Complex off the East Coast of New Zealand's North Island. Although the landslide has been the focus of many studies since first being described by Mountjoy et al. (2009), much remains unknown about the emplacement mechanisms and basal shear zone development. A basal shear zone interpreted in 2D seismic data (Mountjoy et al. 2014) was re-interpreted following the collection of high-resolution 3D seismic data (Gross et al. 2018). Upper and lower landslide units have been identified and characterised within the complex (Gross et al. 2018; Barnes et al. 2019), and the lower unit has been re-interpreted as a submarine fan deposit (Couvin et al. 2020). By combining complementary datasets, we now have the opportunity to compare the intact sediments adjacent to the landslide with the post-failure landslide deposits. Our study addresses the following research aims:

1) Investigate whether there are pronounced physical property contrasts within the intact sediments that might have been exploited for the locus of failure.
2) Explore the origin of the seismic reflections previously interpreted as: a) the basal shear zone of the upper landslide; and b) the base of the lower landslide / fan deposit. Characterise the sedimentological and physical properties across these horizons.

3) Revisit the suggestion (Mountjoy et al. 2014; Gross et al. 2018) that free gas might have played a role in slope destabilisation at this landslide.

2. Geological setting and background

The Tuaheni Landslide Complex, covering an area of ~145 km^2, lies on the upper continental slope of the Hikurangi margin, east of New Zealand (Figure 1). The Hikurangi margin in this region is marked by oblique subduction of the Pacific Plate beneath the Australian Plate at a rate of about 46 mm/year (DeMets et al., 2010). The landslide has been interpreted as a reactivated failure, based on surface morphology that displays a range of morphological expressions of deformation, including lateral shears and concave (downslope) fissures (Mountjoy et al., 2009) (Figure 1b). Mountjoy et al. (2009) and Couvin et al. (2020) provide additional background on the landslide morphology and interpretations of possible emplacement mechanisms. The hummocky seafloor topography forms two distinct lobes – the Northern Lobe and the Southern Lobe that are separated by an intact central ridge (Figure 1b). The central ridge has been interpreted as being composed of contourite deposits, which have partially collapsed into the landslide body during its emplacement (Couvin et al. 2020). Seismic reflectivity within the landslide deposits is generally chaotic, in both sub-bottom profiler acoustic data (Kuhlmann et al., 2019), 2D seismic data (Mountjoy et al. 2009, 2014) and high-resolution 3D seismic data (Gross et al., 2018) (Figure 2), as is typical of mass transport deposits.

[FIGURE PROVIDED SEPARATELY]

*Figure 1. **a**) Regional tectonic setting of New Zealand. HSM = Hikurangi Subduction Margin. **b**) 20 m resolution bathymetry at the Tuaheni Landslide Complex, showing the Northern and Southern Lobes (mbsl = metres below sea level). Blue outline = extent of 3D P-Cable seismic data. The two scientific drill sites are annotated (U1517 and GeoB20802). White lines mark profile locations shown in Fig. 2. Heavy blue lines show locations of sections shown in Fig. 9. **c**) Enlargement from the yellow box in (b) showing root-mean-square (RMS) absolute amplitude in a 15 ms window beneath Reflector H1 and the Intra-debris Reflector (i.e. the reflector that we mark with yellow arrow heads in Fig. 2). For spatial reference to the seafloor, we show the location of the prominent seafloor lateral shear (black line). The patches of high RMS amplitude south of the lateral shear suggest free gas accumulations beneath the base of the upper landslide unit.*

Gross et al. (2018) identified a prominent reflection within the Tuaheni Landslide Complex, the "Intra-debris Reflector" (Figure 2), which they interpreted as the basal shear zone. However, the nature of this horizon and its role in localising deformation remained unclear. The Intra-debris Reflector (termed "R3" by Couvin et al. 2020) marks the base of the upper landslide unit, referred to as Unit II at Site U1517 in Barnes et al. (2019) and Couvin et al. (2020) (Figure 2). Transient-state reaction-transport modelling of pore water data collected through the landslide sequence has indicated that Unit II was emplaced 12.5 ±2.5 thousand years ago (Luo et al. 2020). Beneath the Intra-debris Reflector is Unit III (Figure 2), the unit interpreted as a submarine fan deposit by Couvin et al. (2020). The base of this fan deposit is marked by a prominent, widespread reflection that Gross et al. (2018) referred to as the "Base of Debris Reflector" (termed "R4" by Couvin et al. 2020). Table 1 outlines the published nomenclature for reflectors and lithostratigraphic units.

Table 1. Seismic reflectors and lithostratigraphic units defined in previous studies, and this study

[TABLE PROVIDED SEPARATELY]

The lithostratigraphic units (Table 1) were designated on the basis of sedimentological core analysis at Site U1517 (Barnes et al. 2019). Unit I, from seafloor to 3.0 metres below seafloor (mbsf), is a 3 m thick Holocene sequence of greenish grey silty clay. Unit II, from 3.0 – 40.74 mbsf, is of Late Pleistocene age and the main lithologies are alternating mud (clayey silt to silty clay) and very fine greenish grey sand. Unit III, from 40.74 – 66.38 mbsf, also of Late Pleistocene age, comprises massive

clayey silt to silty clay and alternating layers of dark greenish grey silt and clay. In contrast to Unit II, Unit III contains very little sand.

The intact sedimentary sequence directly adjacent to the landslide deposit has been investigated at drill site GeoB20802 (Figure 1b), which was drilled to 105.4 mbsf using the portable deep-sea drill rig "MARUM-MeBo200", hereafter referred to as "MeBo200" (Huhn, 2016). Huhn (2016) identified three main lithological facies at Site GeoB20802 that they defined as Lithofacies 1 (greenish grey clayey silt), Lithofacies 5 (laminated, sandy, clayey silt) and Lithofacies 6 (disturbed, sandy, clayey silt) (Figure 3a). Further information on these three facies is provided in the *Supporting Information (Text S1)*.

The downslope reaches of the landslide deposit occur in water depths greater than 650 m, where a discontinuous bottom simulating reflection (BSR) marks the base of gas hydrate stability (BGHS) in sediments beneath the slide (Figure 2d) (Gross et al., 2018; Mountjoy et al., 2014). Based on 2D seismic data, Mountjoy et al. (2014) proposed possible links between the gas hydrate system and the slope failure. Gross et al. (2018), in their analysis of 3D seismic data, considered it unlikely that shallow gas hydrates played a role in the Tuaheni Landslide Complex slope failure, but left open the possibility that upward gas migration along faults may have contributed to slope destabilisation. Drilling during International Ocean Discovery Program (IODP) Expedition 372 (at Site U1517, Figure 1b) found no evidence for gas hydrates within the Tuaheni Landslide Complex (Barnes et al. 2019). A recent rock physics study, based on data from Site U1517 and P-Cable seismic data, proposed that gas hydrate saturations of 10-20% exist within the landslide in the upper 30-40 mbsf (Shankar et al. 2020). However, Shankar et al.'s (2020) suggestion can be refuted on the basis that there were no direct visual observations of gas hydrates in sediment cores, nor indirect indications of gas hydrate presence (e.g. chloride or thermal anomalies) anywhere shallower than 100 mbsf at Site U1517 (Barnes et al. 2019). Evidence for gas hydrates from chloride and resistivity anomalies was found in sediments deeper than 100 mbsf at Site U1517 (Screaton et al. 2019; Barnes et al. 2019), but this is much deeper than the landslide units.

3. Data and methods

This study is based on the integration of datasets collected during three research voyages to the Tuaheni Landslide Complex. In 2014, 3D seismic data were collected with a P-Cable system during Voyage TAN1404 aboard *RV Tangaroa* (Böttner et al. 2018 and Gross et al. 2018). In 2016, during Voyage SO247 aboard *RV Sonne*, drill core from the landslide and surrounding undeformed seafloor was collected using MeBo200 (Huhn, 2016). Finally, in late 2017 / early 2018, during IODP Expedition 372 aboard the *JOIDES Resolution*, sediment cores and logging-while-drilling (LWD) data were collected through the landslide complex (Barnes et al. 2019). While the 3D seismic data and the IODP Expedition 372 drilling data have been published previously (Böttner et al. 2018 and Barnes et al. 2019, respectively), data from MeBo200 are presented for the first time in this paper. As such, this paper is the first attempt to correlate these MeBo200 drilling data with the seismic data at the intact sedimentary sequence, and to compare them to IODP drilling data from the landslide deposit.

3.1 Seismic reflection data

The P-Cable seismic data have a trace spacing of 3.125 m within the inlines, and 6.25 m within the crosslines. We estimate the peak vertical seismic resolution ($\lambda/4$) to be approximately 2.5 m, based on near seafloor velocities of 1500 m/s and a dominant frequency of up to 150 Hz. More details about the acquisition and processing of these data are given in Böttner et al. (2018) and Gross et al. (2018).

3.2 Multi-sensor core logger (MSCL), shear strength and sediment core line scans (Site GeoB20802)

Site GeoB20802 (Figure 1b), 546 metres below sea level (mbsl), lies on the undeformed seafloor adjacent to a sidewall scarp of the Tuaheni Landslide Complex. Drill site GeoB20802 was selected as a target because it presented an opportunity to drill through the intact (pre-failure) sequence to a depth greater than the base of the upper landslide. Cores were recovered at this site through a composite of gravity cores for the shallowest section (<10 m) and then two MeBo200 cores (GeoB20802-5 and GeoB20802-6) for the deeper sections. GeoB20802-5 was drilled without coring to 7.4 mbsf and then cored from 7.4 - 31.9 mbsf with a recovery rate of 89%. GeoB20802-6 was drilled without coring to 24.9 mbsf and then cored from 24.9 - 105.4 mbsf with a recovery rate of 95%.

We used a multi-sensor core logger (MSCL) from GEOTEK Ltd at the University of Bremen to make non-destructive measurements of physical properties on sediment cores from Site GeoB20802. We used the archived (split) core sections from this site to measure gamma-ray-attenuated bulk density (ρ), compressional wave velocity (V_p) and magnetic susceptibility (x_m) at 1 cm increments. To correlate V_p and density data from the MeBo200 cores with the P-Cable seismic data, we filtered the V_p and density data to recover the dominant trends. We achieved this by first discarding measurements that fell outside of reasonable data ranges, 1480-2000 m/s and 1500-2500 kg/m^3, for V_p and bulk density, respectively. We then ran a moving average filter over both datasets using a window length of 50 cm, which smoothed small-scale variability while maintaining a vertical sampling rate significantly higher than the vertical resolution of the seismic data. For the shallowest section (<10 m), we interpolated (linearly) our V_p and density curves upward to the seafloor using V_p and density (1512 m/s and 1720 kg/m^3, respectively) from MSCL measurements on the upper 3 m of gravity cores.

We carried out vane shear tests to estimate undrained shear strength at increments of approximately one meter down core on the intact MeBo200 cores. For these tests we used a Wykeham-Farrance laboratory vane apparatus (Model 27-WF1730/2) from the University of Bremen. Finally, we made line scans of the sediment core and we use these images to assist with the correlation of MSCL data and seismic data at key locations down core. Red-green-blue (RGB) values along the line scans provide a quantitative measure of colour variability within the cores, helping to characterise laminations and minor facies changes.

3.3 Logging while drilling (LWD), sediment core physical properties and line scans (Site U1517)

Four holes were drilled at Site U1517 (Figure 1) (Barnes et al. 2019). Hole U1517A was the LWD hole, which advanced to 205 mbsf from a seafloor depth of 722.5 mbsl. Hole U1517B, offset 20 m from Hole U1517A along a heading of 155°, was designated for coring operations but then abandoned after 9.4 m of coring. Hole U1517C, a second attempt at the same location as Hole U1517B, recovered a total of 177.44 m or core from a seafloor depth of 720.9 mbsl down to a sub-seafloor depth of 188.5 mbsf. In this paper, we use published data from Holes U1517A and U1517C (Barnes et al. 2019) to enable core-log-seismic integration with the P-Cable seismic data.

LWD tools attached behind the drill bit at Hole U1517A measured in-situ formation properties (Pecher et al. 2019). V_p was measured using the SonicScope tool with a quadrupole source. Bulk density was measured via the NeoScope tool, a sourceless neutron-gamma density tool. For comparison to the V_p and density LWD data at Hole U1517A, we incorporate other LWD datasets from Hole U1517A as well as physical property measurements made on core from Hole U1517C. The additional LWD datasets that we include are: ring resistivity (geoVISION tool), thermal neutron porosity (NeoScope tool) and

ultrasonic caliper (NeoScope tool). The physical property measurements made on core that we include are natural gamma radiation, magnetic susceptibility, shear strength (automated vane shear device) and moisture and density (MAD)-derived porosity. The reader is referred to Barnes et al. (2019) for detailed descriptions of the datasets and to Pecher et al. (2019) for details on the data collection methods. Finally, we introduce line scan images of sediment core to assist with the interpretation of the LWD and physical property datasets. As with the line scans from Site GeoB20802, we plot RGB values alongside the line scans from Site U1517 to assist with interpretation.

3.4 Log-seismic integration

We completed log-seismic integrations at both drill sites (GeoB20802 and U1517) by depth converting the seismic data using V_p curves from each site. We convolved an estimate of the source wavelet with the reflectivity series determined from the P-wave impedance (Z_p, the product of V_p and density) to generate synthetic data at the drill sites. The source wavelet for this process was estimated using a standard approach in the HampsonRussell software (Russell and Hampson, 1991): "wavelet extraction using a log for constant phase". This approach uses seismic data at the drill site to determine the amplitude spectrum and to generate a zero-phase wavelet. A series of small, constant phase rotations (from -180° to 180°) are then applied to the zero-phase wavelet and a synthetic trace is generated for each rotated wavelet. The wavelet that results in the synthetic trace with the highest cross-correlation with the real trace at the drill site is used as the source wavelet. We also tested a statistical wavelet extraction (zero-phase) from a larger volume of the seismic data and did not notice a significant difference for our log-seismic integration.

3.5 Model-based, post-stack seismic inversion

We used the HampsonRussell software to carry out model-based, post-stack, acoustic impedance inversions in the vicinity of each drill site (Figure 1: blue lines labelled Fig. 9d and Fig 9h). The method is a generalised linear inversion algorithm that iteratively perturbs the starting model until a final model is achieved (Russell and Hampson, 1991; Maurya et al. 2020). The synthetic traces generated by the final model match the real seismic traces as well as possible throughout the inversion time window. Model-based post stack inversions have been used extensively to characterise petroleum systems (e.g. Maurya and Sarkar, 2016), and also shallower gas hydrate systems (e.g. Lee et al. 2013).

We used the stochastic model inversion strategy, where the approach is to minimise, iteratively, the inversion misfit function J given by Equation 1:

$$J = Weight_1(d - W * r) + Weight_2(M - H * r), \qquad (1)$$

where d is the seismic trace, W is the seismic wavelet, r is the final reflectivity, M is the model impedance (determined from filtered log data) and H is the integration operator that convolves with the final P-wave reflectivity to produce the final P-wave impedance. $Weight_1$ and $Weight_2$ are weighting factors between 0 and 1 (where $Weight_1 + Weight_2$ = 1.0) that determine the extent to which the solution is constrained by the background model (i.e. the second term in Equation 1). We tested different weighting values and then chose a value of 0.5 (i.e. $Weight_1 = Weight_2$ = 0.5) for the results presented in this study. In *Supporting Information (Text S2 and Figure S2)* we provide a comparison of different weighting values ($Weight_1$ and $Weight_2$) and the misfit between real and synthetic data.

To build the background model for the inversion we first applied a high cut (10/15 Hz) frequency filter to the P-wave impedance log. This filter removed all frequencies above 15 Hz, yielding a long-

wavelength starting model. This long wavelength structure is essential for the inversion, and has to be recovered from the well log because the low frequencies are always missing from the seismic data (Russell and Hampson, 1991). We constrained the background model away from the well location by using clear seismic horizons in the area of interest. At Site GeoB20802, these horizons were: the seafloor, Reflector H1 (described in the following section), and a horizon deeper than the region of interest, defined simply as the seafloor + 300 ms. At Hole U1517A, we used the seafloor, the Base of Debris Reflector, and (as with at Site GeoB20802) a downward shift of the seafloor reflection (seafloor + 300 ms).

4. Results

4.1 Seismic reflection data

In Figure 2, we present four seismic profiles (Sections w-w', x-x', y-y' and z-z') extracted from the seismic volume that provide an overview of the Tuaheni Landslide Complex. Section w-w' (Figure 2a) runs WNW-ESE along the intact sedimentary section adjacent to the northern sidewall of the slide complex. The sub-seafloor is characterised by several lobes of chaotic reflectivity (white arrows, Figure 2a), suggestive of a local history of repeated sediment remobilization / mass wasting that pre-dates the upper landslide unit (Unit II) of the Tuaheni Landslide Complex. One of these units of chaotic reflectivity (Unit H0) extends through the GeoB20802 drill site (Figure 2a). The dashed white line in Section w-w' marks an onlap surface or angular unconformity that truncates several reflectors, including a prominent reflector that we refer to herein as Reflector H1 (yellow arrow heads, Figure 2a). Drill site GeoB20802, through the undeformed seafloor adjacent to the sidewall (Figure 1b), extends down to a sub-seafloor depth just beneath Reflector H1 (Figure 2a). Anomalously high-amplitude reflections occur in some places, suggestive of localised free gas accumulations (Gross et al. 2018) (Figure 2a, selected examples labelled).

[FIGURE PROVIDED SEPARATELY]

Figure 2. Seismic sections through the Tuaheni Landslide Complex (see Fig. 1b for locations). Vertical axes in seconds (s) two-way travel time (TWT). "VE" = vertical exaggeration. ***a) Section w-w'****) Section along the intact seafloor adjacent to the sidewall. Annotated are: Reflector H1 (yellow arrow heads), the GeoB20802 drill site, and example high-amplitude patches that we interpret as free gas (see example enlarged wavelet compared to the seafloor wavelet). White arrows point to lobes of incoherent seismic reflectivity, including one lobe that we define as "Unit H0".* ***b) Section x-x'****) Inline 648, crossing the Northern Lobe of the slide. Annotated are: Reflector H1 and the Intra-Debris Reflector (IR), after Gross et al. (2018). Lateral continuity, as well as consistent amplitude and phase (see yellow boxes), means we correlate Reflector H1 (beneath the intact seafloor) to the Intra-Debris Reflector. We annotate both by yellow arrow heads. Cyan arrow heads mark the Base of Debris (BD), after Gross et al. (2018).* ***c) Section y-y'****) Section through the Northern Lobe of the landslide. Annotations as in (b).* ***d) Section z-z'****) Composite seismic line running from north of GeoB20802, southwest across the Northern Lobe, and then southeast along the Southern Lobe and through drill site U1517. Annotations as in other sections above. Dotted white lines on left-hand side of the section indicate the 15 ms window beneath Reflector H1, within which root-mean-square amplitudes were extracted for the plot in Fig. 1c. Dashed white line on the right-hand-side of the section marks the approximate base of gas hydrate stability (BGHS) (Gross et al. 2018; Barnes et al. 2019).*

In Section x-x' (Figure 2b), Reflector H1 can be traced to the sidewall scarp, where it occurs at the same stratigraphic depth as the Intra-debris Reflector, which has been interpreted as the base of the upper landslide unit (Unit II) (Gross et al. 2018). The amplitude and phase of Reflector H1 is consistent with that of the Intra-debris Reflector (Figure 2b, enlarged yellow boxes). A deeper reflection at the base of Unit III is marked by cyan arrow heads; this reflection was termed the Base of Debris Reflector by Gross et al. (2018) (Figure 2b).

Section y-y' (Figure 2c) is a section running approximately NW-SE through the Northern Lobe of the landslide complex. The Intra-debris Reflector is clearly identifiable in the Northern Lobe. Example

interpretations of free gas accumulations are annotated, including directly beneath the upper landslide unit, Unit II (Figure 2c).

Section z-z' (Figure 2d) links Site GeoB20802 in the North to Site U1517 in the South. A central ridge divides the Northern and Southern Lobes (Figures 1b, 2d). The Intra-debris Reflector is generally not as prominent in the Southern Lobe of the landslide as it is in the Northern Lobe. Indications of free gas are also widespread in this composite profile, including directly beneath the upper landslide unit, Unit II (Figure 2d). Although gas appears to accumulate directly beneath the upper landslide unit in several places, there are no clear indications for gas accumulating beneath Reflector H1, the lateral continuation of the Intra-debris Reflector into the pre-slide stratigraphy north of the sidewall (Figure 2d). This is demonstrated in the map of root-mean-square amplitudes in Figure 1c, extracted in a 15 ms window beneath Reflector H1 and the Intra-debris Reflector (Figure 2d). This map highlights the spatial distribution of strong reflectivity (high root-mean-square amplitudes) likely caused by gas that exists just below the Intra-debris Reflector. This suggests there is a preference for gas to be trapped beneath the landslide (i.e. south of the lateral shear), but not at equivalent sub-seafloor depths north of the lateral shear and beneath the intact seafloor (Figure 1c).

4.2 Site GeoB20802

4.2.1 Undrained shear strength and MSCL data

Undrained shear strength at Site GeoB20802 are presented in Figure 3b. A linear fit through the data is used to highlight depth intervals where the undrained shear strength deviates from the background trend. Note that this linear fit is anchored at the shallowest measurement close to the seafloor. Undrained shear strength increases relatively steadily from around 10 kPa close to the seafloor to a value of ~55 kPa at a sub-seafloor depth of 42 mbsf (Figure 3b). From 42 to 72 mbsf, shear strength values vary between 25-55 kPa. This range (25-55 kPa) persists in general down to the bottom of the core at 105 mbsf, with notable exceptions that there are pronounced undrained shear strength peaks at approximately 76, 84 and 91 mbsf, and again at the bottom of the core (105 mbsf). Likewise, there are four intervals in the lower half of the borehole where multiple successive undrained shear strength measurements are lower than the background linear trend; these occur in the depth intervals 67-72, 78-81, 85-88 and 92-101 mbsf.

[FIGURE PROVIDED SEPARATELY]

*Figure 3. Log-seismic integration at Site GeoB20802 (178° 28.96', -38° 45.93'; Inline 650, Crossline 6210). **a)** Lithofacies after Huhn (2016). Lithofacies 1 = greenish grey clayey silt; Lithofacies 5 = laminated, sandy, clayey silt; Lithofacies 6 = disturbed, sandy, clayey silt. Horizontal green ticks mark depths of thin (<5 cm) tephra beds identified within the core. **b)** Undrained shear strength (S_u) (kPa). mbsf = meters below seafloor. Empty circles (down to ~32 mbsf) and filled dots (the rest) are data points from GeoB20802-05 and GeoB20802-06, respectively. Broken red line is a linear trend line anchored at the shallowest measurement (10.54 kPa). Equation of line given in red. Peach-coloured intervals highlight local strength peaks in the lower 30 m of the core, which generally correlate to bulges in density (see panel c). The local strength peaks around 90 mbsf and 104 mbsf (bottom of the core) also correlate to step increases in V_p (see panel b). A comparison of these S_u data to a global compilation (Sawyer and DeVore, 2015) is given in the Supporting Information (Text S3 and Figure S3). **c)** P-wave velocity (V_p) (m/s) measured with the multi-sensor core logger (MSCL). Grey dots = raw data. Blue line = running mean. **d)** Bulk density (ρ) (kg/m³) measured with the MSCL. Grey dots = raw data. Blue line = running mean. **e)** Magnetic susceptibility (X_m) from the MSCL. **f)** P-wave impedance (Z_p): product of the running means of V_p (b) and ρ (c). Heavy black ticks next to all sub-figures show locations of line-scan images shown in Figs. 4 and 5. **g)** Seismic data at the drill site, vertical axes in milliseconds two-way time (TWT) as well as mbsf. Depth conversion based on blue V_p curve in (b). H1 = Reflector H1. Unit H0 (from ~75 to ~95 mbsf) labelled. **h)** Comparison between synthetic traces (left) and P-Cable traces (right) at the borehole. H1 = Reflector H1. Dotted ellipses encircle two synthetic waveforms that do not correlate well with the P-Cable data. Cross-correlation value (0.8) refers to range between the yellow lines. Note: no squeezing/stretching was applied to improve the cross-correlation at this site.*

The raw and filtered V_p data are displayed in Figure 3c. Like the undrained shear strength profile, V_p increases relatively steadily to a depth of ~42 mbsf. There is a distinct V_p drop at ~42 mbsf, and an even more pronounced drop (on the order of ~130 m/s) at ~50 mbsf. A low velocity zone extends from ~50 to ~89 mbsf, at which depth V_p then steps up again (by ~140 m/s). V_p remains at approximately 1700 m/s below 90 mbsf, before increasing to higher velocities beneath about 101 mbsf.

The bulk density data (Figure 3d) display pronounced inflections in many intervals down core, including at ~50 mbsf, where there is also a significant drop in V_p. From ~70 mbsf downward, the bulk density increases from ~1800 to ~2200 kg/m^3. Throughout this depth interval (i.e. the lowermost 35 m of the cored section), there is a fluctuating density trend with peak to peak cyclicity on the order of ~7 m. Density peaks throughout this fluctuating interval correlate with the intervals where undrained shear strength is relatively high. We have demonstrated this alignment between bulk density maxima and intervals of increased undrained shear strength by the horizontal, peach-coloured bars in Figure 3.

Finally, and for reference, magnetic susceptibility data are shown in Figure 3e. Local bulk density maxima generally correlate with intervals of higher-than-background magnetic susceptibility, such as in the interval from ~81-83 mbsf, the interval around 90 mbsf (also where the pronounced V_p step is), and near the bottom of the core (~102-104 mbsf).

4.2.2 Log-seismic integration

The log-seismic correlation at Site GeoB20802 is represented in Figure 3, where the seismic data around the drill site (Figure 3g) are depth converted using the velocity profile in Figure 3c. The correlation between synthetic seismic traces and P-Cable seismic traces at the drill site is shown in Figure 3h. The deepest reflection captured by the log-seismic integration is Reflector H1, a negative polarity event beneath 850 ms two-way time (TWT) (Figure 3h). Two positive-polarity synthetic reflections (between 830 and 850 ms TWT, Figure 3h) are exceptions to what is otherwise a good cross correlation between the P-Cable and synthetic seismic data. These two synthetic reflections lie within a chaotic, low-amplitude seismic unit above Reflector H1 – the unit that we have designated as Unit H0 (Figures 2a, 3g, and Table 1).

4.2.3 Line-scan images

Figures 4 and 5 present a selection of line-scan images, and corresponding RGB intensity, from sediment core recovered from Site GeoB20802. The depth intervals of all line scans are shown by horizontal black ticks in Figure 3. In general, sediments throughout this drill site are characterised by greenish grey, clayey silt. However, distinct variations occur down-core, including depth intervals characterised by dark silt laminations (e.g. Figures 4b, 4g, 5a), distinct colour changes (e.g. Figures 4c, 5a, 5e, 5g), irregular / contorted laminations (Figures 4c, 4d), divergent or "fanning" laminae (Figure 5c), and core disturbance caused by gas expansion (Figures 5d-f).

[FIGURE PROVIDED SEPARATELY]

Figure 4. Line-scan images of sediment core at selected locations down core at Site GeoB20802 (see Fig. 3 for locations). Beneath each line scan are red-green-blue (RGB) values along the scans. Depth labels on the tops of line-scan images are in meters below seafloor (mbsf). Various features in the core are annotated (see text for further descriptions).

[FIGURE PROVIDED SEPARATELY]

Figure 5. Line-scan images of sediment core at selected locations down core at Site GeoB20802 (see Fig. 3 for locations). Beneath each line scan are red-green-blue (RGB) values along the scans. Depth labels on the tops of line-scan images are in meters below seafloor (mbsf). Various features in the core are annotated (see text for further descriptions).

The pronounced V_p inversion at ~52 mbsf (Figure 3c) correlates to a 2 cm-thick silt turbidite and a facies change (Figures 3a, 4b) – the sediment below 52 mbsf becomes laminated and darker coloured (Figure 4b; lower RGB values). At ~60 mbsf, seismic reflectivity changes from high-amplitude and laterally-continuous to lower-amplitude and less laterally coherent (Figure 3g). This less coherent seismic facies beneath 60 mbsf correlates to sedimentary units characterised by irregular and contorted laminations within the core (e.g. Figures 4c,d). The peak shear strength at ~75.7 mbsf (Figure 3b) correlates to a darker clay-rich interval underlain and overlain by silt layers (Figure 4e). The pronounced V_p increase around 90 mbsf (Figure 3c) corresponds to divergent laminae in the core (Figure 5c), suggestive of folding / shearing. Deeper in the borehole, below ~91 mbsf, we observed frequent gas expansion fractures in the core (e.g. Figures 5d-f) that occurred during de-pressurisation as the cores were recovered and gas came out of solution from the pore fluid. Beneath the gas expansion features, in Core Section 24P-3A, is a 3 cm-thick, graded coarse silt layer, which also manifests itself as a darkening of colour (a drop in RGB values; Figure 5f). This is the most distinct feature that we observed in the vertical vicinity of Reflector H1, and it is underlain by faintly laminated, stiff, clay-rich silt (Figure 5g).

4.3 Site U1517

4.3.1 Logging while drilling (LWD) data and log-seismic integration (Hole U1517A)

Ultrasonic caliper measurements (borehole diameter), ring resistivity, neutron porosity, V_p and neutron density for the upper 72 m at Hole U1517A are displayed in Figure 6a-e. This depth range includes both the Intra-debris Reflector and the Base of Debris Reflector (Gross et al. 2018) (Figure 6h). For reference, we also plot P-wave impedance (Z_p) (Figure 6f) and include the interpreted LWD logging units defined by Barnes et al. (2019) (Figure 6g).

[FIGURE PROVIDED SEPARATELY]

Figure 6. Log-seismic integration at Hole U1517A (178° 28.5574', -38° 49.7722'; Inline 1776, Crossline 4225). **a)** Ultrasonic caliper measurement of borehole diameter (inches). Mbsf = meters below seafloor. **b)** Ring resistivity (Ω m). **c)** Neutron porosity (φ). **d)** P-wave velocity (V_p) (m/s) (blue). Dotted black line = projected V_p through "washout" zone, where measurements were compromised (see text for more detail). Broken red line = V_p log after stretching to generate the synthetic shown in (i). **e)** Neutron density (ρ) (kg/m^3). Dotted black line = projected density through washout zone. **f)** P-wave impedance (Z_p) (m/s x kg/m^3). **g)** Logging units (1-4), defined by Barnes et al. (2019). **h)** P-Cable seismic data at the drill hole, with vertical axes in milliseconds two-way time (TWT) as well as mbsf. Depth conversion based on the V_p curve in (d) (broken red line). "IR" and "BD" (dotted yellow lines) are the Intra-debris Reflector and the Base of Debris Reflector, respectively (see e.g. Fig. 2). **i)** Comparison between synthetic traces (left) and P-Cable traces (right) at the borehole. Minor stretching to align reflections resulted in the slight change to the V_p curve shown in (d). The extent of the Intra-debris Reflector and Base of Debris Reflector wavelets are shown next to the P-Cable traces.

A washout zone in the interval from 22 to 28 mbsf is indicated by the extremely high porosity, low V_p and low density (Figure 6c-e). Washout zones are presumably related to the existence of non-cohesive sediments (silt to sand) with low clay content (Barnes et al. 2019). To avoid compromising the log-seismic integration, and in particular the time to depth conversion, we deleted bulk density, V_p and Z_p values within the washout zone (22-28 mbsf) and interpolated linearly from 22 – 28 mbsf (dotted red lines, Figure 6d-f). The log-seismic correlation at Hole U1517A is represented in Figure 6h, where the seismic data around the drill site are depth converted using the velocity profile in Figure 6d. The correlation between synthetic traces and P-Cable traces at the drill site is shown in

Figure 6i. The most pronounced sub-seafloor reflection in the P-Cable data is the Base of Debris Reflector at ~1025 ms TWT (Figure 6h). This reflection correlates well to a pronounced positive polarity synthetic reflection that arises from the Z_p increase between 55 and 60 mbsf (i.e. LWD Unit 3b; Figures 6f,g), providing good control on the log-seismic integration. The Intra-debris Reflector (Figure 6h) is much subtler than the Base of Debris Reflector, and the correlation between synthetic and P-Cable data is not as good in the depth vicinity of the Intra-debris Reflector (Figure 6i).

4.3.2 Core-seismic integration from physical property measurements at Hole U1517C

Hole U1517C (Figure 7) lies on the same seismic inline as Hole 1517A (the LWD hole), but 20 m downslope. We here present the lithological log and lithostratigraphic units (Figures 7a,b) (Barnes et al. 2019), alongside undrained shear strength, RGB values from line scans, natural gamma radiation, MAD-derived porosity, and magnetic susceptibility (Figures 7c-g).

[FIGURE PROVIDED SEPARATELY]

Figure 7. Physical property measurements made on the upper 70 m of sediment core at Hole U1517C (178° 28.5633', -38° 49.7820'; Inline 1776, Crossline 4219). **a and b)** Lithological log and major lithostratigraphic units from Barnes et al. (2019) (legend at bottom). Mbsf = meters below seafloor. Note: lithostratigraphic units I-IV (shown here) are distinct from the logging units (1-4) shown in Figure 6 (Barnes et al. 2019). Grain size analyses from samples at this hole are provided in the Supporting Information (Text S4, Figure S4). Black and grey boxes indicate depth intervals of line scan images shown in Figure 8. **c)** Undrained shear strength (S_u) (kPa) (black dots are from vane shear, blue dots are from a penetrometer). Broken red lines are linear trend lines calculated for data above and below 24 mbsf – the approximate depth where there is a clear change in the data trend. Equations of the lines are given in red. A comparison of these S_u data to a global compilation (Sawyer and DeVore, 2015) is given in the *Supporting Information (Text S3 and Figure S3)*. **d)** Red-green-blue (RGB) values from line scans. **e)** Natural gamma radiation (NGR) (counts/s). **f)** Moisture and Density (MAD)-derived porosity (φ) (dimensionless). **g)** Magnetic susceptibility (X_m) (dimensionless). **h)** P-Cable seismic data at the drill site (U1517C, vertical black line), with vertical axes in milliseconds two-way time (TWT) and mbsf. Our depth conversion is based on the same sub-seafloor velocities used at Hole U1517A (dotted red line) (see Figure 6). "IR" and "BD" (dotted yellow lines) are the Intra-debris Reflector and the Base of Debris Reflector, respectively (see e.g. Fig. 2). Thin vertical blue line is the location of the LWD hole, Hole U1517A (from Figure 6h).

The Base of Debris Reflector (Figure 7h) occurs within the lower part of Lithostratigraphic Unit III, represented by the distinct drop in MAD porosity and RGB values between ~61 and ~66 mbsf. This ~5 m thick interval of lower MAD porosity is the equivalent of the reduction in neutron porosity in Logging Unit 3b at the LWD site (Hole U1517A, Figure 6). The Intra-debris Reflector (Figure 7h) appears to correlate to the boundary between lithostratigraphic Units II and III (Figures 7b, h), where there is also a distinct change in magnetic susceptibility (Figure 7g) and RGB value scatter (Figure 7d).

Undrained shear strength increases steadily from the seafloor down to a depth of approximately 24 mbsf (Figure 7c), within Unit II. Between 12 and 24 mbsf, shear strength regularly exceeds values of 100 kPa – values that were not measured anywhere down core in the 105 m of sediments adjacent to the landslide at Site GeoB20802 (Figure 3b). Below 24 mbsf at Hole U1517C, shear strength drops back to values that are typically less than 100 KPa (Figure 7c). Aside from the upper 5 mbsf, the lowest shear strength measurements occur at ~30 mbsf (Figure 7c). This depth broadly correlates with an interval of scattered RGB values (Figure 7d), a local reduction in natural gamma radiation (Figure 7e) and a local increase in MAD porosity (Figure 7f). Notably, this marked reduction in shear strength at ~30 mbsf is well above (i.e. ~10 m shallower than) the Intra-debris Reflector. As with Site GeoB20802, we have added linear trend lines to the undrained shear strength data to highlight deviations from the background trend (Figure 7c). We have calculated separate trend lines for the data above and below 24 mbsf because of the pronounced change at this depth.

4.3.3 Line scan images (Hole U1517C)

Figure 8 shows example line scan images at selected locations down hole. We focus on the lower part of Unit II, and the boundary between Unit II and Unit III (see depth intervals annotated to Figure 7). The darker bands within the line scans in Figure 8 represent sandy layers. There is a distinct increase in the thickness of the sandy intervals from about 30 mbsf (Figure 8), which coincides with the reduction in natural gamma radiation and the region of more scattered RGB values in the depth vicinity of 30-35 mbsf (Figure 7d,e).

[FIGURE PROVIDED SEPARATELY]

Figure 8. Line-scan images of sediment core at selected locations down core at Hole U1517C (see Fig. 7 for depth intervals). Beneath each line scan are red-green-blue (RGB) values along the scans. Depth labels on the tops of line-scan images are in meters below seafloor (mbsf), using the IODP Core Depth Below Seafloor B (CSF-B) scale. Some features in the core are annotated (see text for further descriptions).

Figures 8f-8i span the depth interval 37.7 – 42.4 mbsf, across the boundary between Unit II and Unit III (Figure 7). The most distinct change in the core across this boundary is the absence of sandy intervals beneath ~39.5 mbsf (Figure 8). There is also a distinct increase in magnetic susceptibility from ~39.5 mbsf downward (Figure 7g), and RGB values become less scattered (Figure 7d).

4.4 Post-stack acoustic inversion for P-wave impedance (Z_p) around the drill holes

The Z_p logs at Sites GeoB20802 (Figure 3f) and U1517 (Figure 6f), combined with an estimate of the source wavelet (Figure 9a,b), provide the opportunity to invert for Z_p in the regions surrounding each drill site. We present representative inversion results at both drill sites in Figure 9. In *Supporting Information (Figure S2)* we show additional inversion results at Site U1517 based on different weighting factors (see also description in Section 3.5) to demonstrate the relatively minor effect of weighting factors on the final Z_p inversion results.

[FIGURE PROVIDED SEPARATELY]

Figure 9. P-wave impedance (Z_p) inversions at Sites GeoB20802 and U1517. **a)** Source wavelet used for the inversions, estimated statistically from ~360,000 traces in the seismic data volume. **b)** Frequency domain of source wavelet. **c)** Z_p (black line) at Hole GeoB20802. Cyan line = filtered Z_p (high cut; 10/15 Hz) used as starting model. H1 = Horizon 1. **d)** P-Cable seismic data around Site GeoB20802 (see Fig. 1b for location). Vertical blue line represents the drill hole. Red dash ~halfway down the drill hole marks a negative polarity reflection associated with a pronounced impedance drop. **e)** Z_p inversion of data in (d). Identical scale, extent and labels as (d). Red dash as in (d), marking the pronounced impedance drop at this depth. Impedance increases again within Unit H0. Results at stratigraphic depths deeper than the bottom of the drill hole are masked, due to the lack of well control. **f)** Comparison between P-Cable and synthetic data (from Z_p inversion), at Site GeoB20802. **g)** Z_p (black line) at Hole U1517A. Cyan line = filtered Z_p used as starting model. BD = Base of Debris Reflector; BGHS = approximate base of gas hydrate stability. **h)** P-Cable seismic data around Site U1517 (see Fig. 1b for location). IR (black arrows) = Intra-debris Reflector; BD (magenta arrows) = Base of Debris Reflector. **i)** Z_p inversion of data in (h). Identical scale, extent and labels as (h). **j)** Comparison between P-Cable and synthetic data (from Z_p inversion) at Site U1517.

Our inversion around Site GeoB20802 is shown in Figure 9c-f. A negative polarity reflection approximately half way between the seafloor and the bottom of the drill hole (shown by the red dash in Figure 9d) is a result of the impedance drop at ~50 mbsf (795 ms TWT) (Figure 3f). This impedance drop is well recovered away from the drill hole in the inversion results of Figure 9e. Deeper beneath the seafloor, within Unit H0, Z_p begins to increase again with depth, from values of ~3.0 to ~3.5 (km/s x g/cm^3) (Figure 9e).

Our inversion around Site U1517 is shown in Figure 9g-j. The results reveal pronounced low-Z_p layers that dip to the NW beneath the regional BGHS. These represent gas-charged layers beneath the gas hydrate system (Gross et al. 2018), where free gas drastically reduces the velocity of the host strata (e.g. Domenico, 1976). The sediments between the seafloor and the Base of Debris Reflector are characterised by relatively high Z_p, when compared with deeper sediments that lie between the Base of Debris Reflector and the BGHS (Figure 9h). Z_p is locally high at the Base of Debris Reflector (Figure 9i), consistent with the increase in both V_p and density in this depth interval that was noted in the LWD data (i.e. between 55 and 60 mbsf, Figure 6d,e). The weakly-reflective, negative-polarity Intra-debris Reflector (Gross et al. 2018) correlates to a subtle drop in Z_p (Figure 9i, yellow to green colours) around 500 ms beneath the seafloor. This Z_p drop correlates to the depth within core at Site U1517C where interbedded sandy intervals cease to exist beneath a depth of ~39.5 mbsf (Figure 8).

5. Discussion

5.1 The intact sedimentary sequence (Site GeoB20802) adjacent to the landslide

Site GeoB20802 cored through Reflector H1, which appeared (in seismic data at least) to represent the intact lithological unit / boundary that became the failure surface of the upper landslide. Synthetic seismic data generated from V_p and density measurements on the core have reproduced the negative polarity Reflector H1 near the base of the drill hole (Figure 3h). Indeed, the log-seismic correlation at this site, based on smoothed MSCL data, is very good through most of the length of the drill hole (cross-correlation of 0.8, Figure 3h). However, there are two clear exceptions within the chaotic unit (Unit H0), where pronounced synthetic reflections are generated that do not correlate well to the P-Cable data (Figure 3h). The upper synthetic reflection (annotated by the upper ellipse in Figure 3h) correlates to a local increase in density just below 80 mbsf (Figure 3d). The lower synthetic reflection (annotated by the lower ellipse, Figure 3h) correlates to a pronounced increase in V_p (Figure 3c) and an increase in density (Figure 3d) at around 90 mbsf, which align with the zone of dark fanning laminae in Figure 5c. While the point sampling nature of sediment coring forms the basis for these pronounced impedance contrasts, we speculate that they are not sufficiently laterally continuous to generate coherent reflections in the seismic data. Given the chaotic character of Unit H0, we interpret it as a buried mass transport deposit. This interpretation is supported by contorted and divergent laminations in some of the darker intervals of the core (Figures 4c,d and 5c), which point to sub-parallel deformation and potentially even folding of the primary sedimentary structure. It is important to note that this interpreted mass transport deposit (Unit H0) was emplaced long before the Tuaheni Landslide Complex – Unit H0 is covered by at least 60 m of laterally continuous reflections (Figure 3g). Unit H0 is just one example of what appears to be a complex spatial pattern and history of mass wasting on the slope (white arrows, Figure 2a).

Given that the highly variable undrained shear strength beneath ~75 mbsf correlates to Unit H0 (Figure 3), we interpret that this strength variability was inherited during emplacement of this (now buried) mass transport deposit. The correlation between undrained shear strength and bulk density fluctuations in Unit H0 indicates that there is an inherent relationship between bulk density and undrained shear strength. In general, the denser intervals correspond to the darker, laminated intervals in the core while the less dense intervals correlate to the lighter, more homogenous intervals.

Despite the detail revealed by core-log-seismic integration, we cannot unequivocally attribute a particular weak layer (or layers) beneath the seafloor at Site GeoB20802 to the basal shear zone of

the Tuaheni Landslide Complex's upper landslide unit. Because Reflector H1 can be traced from the intact sequence to beneath the landslide, where its polarity and amplitude remain essentially unchanged (Figure 2b), we suggest that the sediment layering responsible for this reflection has remained intact beneath the upper landslide. In other words, the basal shear zone likely developed distinctly above Reflector H1 (Figure 3g). The closest interval of low undrained shear strength that is clearly above Reflector H1 is the interval from 85-88 mbsf (Figure 3b) that lies directly above the pronounced step increase in Z_p at ~90 mbsf (Figure 3f). Another relatively weak interval exists between 78 and 81 mbsf, while the most pronounced weak interval occurs significantly shallower in the sedimentary sequence (67-72 mbsf). Any of these intervals, and perhaps all of them, could have been exploited as shear zones of the upper Tuaheni Landslide, at least in the Northern Lobe of the complex. We note that undrained shear strength measurements on remoulded samples can, in some cases, provide additional insight into the lower bound strength of landslide materials (Kvalstad et al. 2005b). However, such a comprehensive geotechnical analysis is beyond the scope of this study.

As with most submarine landslide investigations, there are several possible pre-conditioning and triggering factors that could be relevant for the creation of the Tuaheni Landslide Complex. Without any measurements of pore fluid pressure at the GeoB20802 site, we can only speculate as to whether pore fluid pressure at the boundaries between the more laminated and more homogenous sediment intervals in Unit H0 (e.g. Figures 4g and 5b, respectively) might have played a role in the failure. Pore pressure accumulation at the boundaries between different lithologies is a process that has been proposed elsewhere for subaqueous slope failures (e.g. Stegmann et al. 2007; Urlaub et al. 2018). In the similar tectonic setting of the Nankai forearc, earthquake shaking and pore fluid pressure have been invoked as likely landslide triggers (e.g. Strasser et al. 2011), where wedge-scale transient fluid pressure conditions have been interpreted on the basis of dilatational and compactional structures in fault zones (Conin et al. 2014). Given the location of the Tuaheni Landslide Complex atop an active subduction margin, earthquake shaking and/or any associated pore pressure change may have destabilized a weak layer (or layers). Sources of significant ground shaking could come from shallow crustal faults, intraslab faults, and the subduction interface (e.g. Reyners, 1998; Holden et al. 2008; Stirling et al. 2012). Notably, transient fluid expulsion has also been interpreted in the region of the Tuaheni Landslide Complex on the basis of seafloor heat flow measurements (Pecher et al. 2017). Building on these studies, Carey et al. (2020) have investigated the potential movement mechanisms of the Tuaheni Landslide Complex during earthquakes. Using undrained dynamic shear experiments, they show that the coarse silt to fine sand sediments are unlikely to liquify within the low-angle basal shear zone of the landslide. They concluded that a basal frictional failure mechanism is more likely, when pore water pressures are sufficiently increased during earthquake shaking.

Our demonstration that free gas exists directly beneath the base of the Northern Lobe, but not at the same stratigraphic level below the undeformed seafloor (Figure 1c), can be interpreted in two different ways. On the one hand, the free gas directly beneath the landslide may have existed prior to the initial slope failure, thereby playing a role in reducing effective stress and destabilising the slope. On the other hand, free gas directly beneath the landslide could be the result of some upward-migrating gas becoming trapped beneath the landslide after it was emplaced. This latter scenario is possible because landslide deposits can behave as seals to upward gas flow (e.g. Cardona et al. 2016; Sun et al. 2017; Moernaut et al. 2020), since they are typically denser than surrounding, undisturbed strata (e.g. Sawyer et al. 2009). Indeed, our seismic inversion results around Site U1517 (Figure 9i) demonstrate the increase in Z_p (both density and velocity) within the shallow landslide units,

compared to the sediments deeper than the Base of Debris Reflector. The Base of Debris Reflector itself is the direct seismic response to localised densification / porosity reduction at the base of the lower landslide unit, Unit III (Figures 6 and 7). In any case, there is widespread evidence from negative polarity seismic amplitude anomalies for gas charged strata in the sub-seafloor of the greater Tuaheni region (Mountjoy et al. 2014; Micallef et al. 2015; Gross et al. 2018). Micallef et al. (2015) proposed that early-stage spreading failures just 15 km to the Northeast of the Tuaheni Landslide Complex were caused by the presence of shallow gas. Higgs et al. (2019) documented widespread, active, and long-lived gas seepage just upslope of these spreading failures. Together, these previous studies, and the indications for widespread gas in the subsurface beneath the Tuaheni Landslide Complex (e.g. Figure 2), indicate that free gas may have played a role in pre-conditioning the slope for failure.

5.2 The Tuaheni Landslide Complex sediments (Site U1517)

Our core-log-seismic integration at Site U1517 provides the opportunity to address previous interpretations of the Tuaheni Landslide Complex (e.g. Mountjoy et al. 2014; Gross et al. 2018; Couvin et al. 2020), as well as draw comparisons to the intact sedimentary sequence at Site GeoB20802.

The drilling results confirm the absence of gas hydrates within the shallow landslide units (Barnes et al. 2019), as Gross et al. (2018) had inferred on the basis of 3D seismic interpretation. This conclusively rules out a hypothesis proposed by Mountjoy et al. (2014) that gas hydrates have directly altered the rheology of the landslide, thereby causing present-day downslope creep. An alternative interpretation in Mountjoy et al. (2014), referred to as a "gas-valve" hypothesis, suggested that hydraulic fracturing or fault reactivation could transport free gas toward the shallower landslide and thereby reactivate it through overpressure accumulation. This general mechanism (Flemings et al. 2003; Hornbach et al. 2004) has also been proposed for slope failure and seafloor erosion elsewhere, and modelled theoretically (e.g. Crutchley et al., 2010; Elger et al., 2018). This gas-valve mechanism remains untested for the specific conditions at the Tuaheni Landslide Complex (i.e. *in situ* stresses and gas pressures) but is the focus of ongoing research that is beyond the scope of this paper.

Gross et al. (2018) identified and mapped out the Intra-debris Reflector and the Base of Debris Reflector in both the Southern and Northern Lobes of the Tuaheni Landslide Complex. As mentioned above, the Base of Debris Reflector is clearly linked to densification and velocity increase at the base of Lithostratigraphic Unit III / LWD Unit 3 (Figures 6 and 7) – the unit interpreted by Couvin et al. (2020) as a submarine fan deposit. The Intra-debris Reflector is difficult to constrain at Hole U1517A, because our log-seismic integration in this interval of the drill site does not correlate as well with the P-Cable data (Figure 6i). The best insight we can gain into the origin of the Intra-debris Reflector comes from the sediment cores at Hole U1517C and, in particular, the boundary between Lithostratigraphic Unit II and Unit III (Figure 7). The transition from Unit II to III, around 40 mbsf, correlates with the approximate sub-seafloor depth of the Intra-debris Reflector. From this depth downwards, the most noticeable lithological change in the core is the lack of very fine – medium sand layers (Figure 7a), which manifests itself as a less scattered distribution of RGB values (Figure 7d) and an increase in magnetic susceptibility (Figure 7g). The deepest sandy interval in Unit II ends at 39.3 mbsf (Figure 8g) – below this depth are clay intervals interbedded with silt layers (Figure 8g-i). This change from sandy intervals existing (above) to sand intervals being absent (below) is a likely explanation for the negative polarity of the Intra-debris Reflector, since sands typically have higher

velocities than surrounding clays in shallow sub-seafloor sediments (Cook and Sawyer, 2015). Our core-log-seismic integration at Site U1517 therefore supports the previous interpretation that the Intra-debris Reflector separates two distinct units, with the deeper Unit III having a different depositional origin to the more recent Unit II (Couvin et al. 2020).

In contrast to an interpretation of Gross et al. (2018) that the Intra-debris Reflector might represent an induced shear zone at the base of the upper landslide, there is no evidence for a distinct change in undrained shear strength in the depth vicinity of the Intra-debris Reflector (Figure 7). Rather, the pronounced reduction in shear strength within the upper landslide unit (Unit II) starts at ~25 mbsf (Figure 7c), approximately 15 m shallower than the Intra-debris Reflector. Comparison of physical property data from cores (Figure 7, Hole U1517C) with the LWD data (Figure 6, Hole U1517A) suggests that the washout zone at Hole U1517A (around 22-28 mbsf, Figure 6) may correlate to the reduction in undrained shear strength that begins at ~25 mbsf at Hole U1517C (Figure 7c). As such, it seems likely that the localised reduction in undrained shear strength has developed within the upper landslide unit during emplacement – i.e. an induced weak layer, following the terminology of Locat et al. (2014). It is not possible to correlate this weak zone directly to the intact sequence because of the large geographic separation between Sites U1517 and GeoB20802 (Figure 1b). However, our interpretation that the Intra-debris Reflector remained intact during landslide emplacement (see Section 5.1) is consistent with the inference that the landslide induced a weak interval distinctly above the Intra-debris Reflector. Some ongoing research at the Tuaheni Landslide Complex is based on numerical modelling of slope failure, which should consider potential weak layers in both the intact sequence (at Site GeoB20802) and within the landslide body (Site U1517).

5.3 Core-log-seismic integration outlook

The integration of sediment core data, logging data and seismic reflection data is an approach that is commonly used in the petroleum industry and in geoscience research (e.g. Mitchum et al., 1993; Bloomer and Mayer, 1997; Riedel et al. 2020). Subaqueous landslide investigations are well-suited to this type of approach, where small-scale measurements and observations from drill holes need to be put into context of large-scale geology – scales that can only be investigated using seismic reflection data. Our study has demonstrated the value of combining datasets from remote seafloor drilling (MeBo200 system), ship-based drilling (*JOIDES Resolution*) and 3D seismic surveying (P-Cable system). In particular, we showed that P-wave velocity and density measurements, made with a MSCL on sediment core recovered with MeBo200, can be used for a robust integration with seismic reflection data (Figure 3). While it is more common to use LWD or wireline data for log-seismic integrations, such datasets are not always available. Our study, together with a recent study of Danube Deep Sea Fan sediments (Riedel et al. 2020), highlights the value of combining P-Cable 3D seismic data with MSCL data from MeBo200 drill cores for such core-log-seismic integration studies.

6. Conclusions

In this study we have integrated a diverse set of geological and geophysical datasets at the Tuaheni Landslide Complex to characterise both the intact sedimentary sequence (Site GeoB20802) and the landslide sediments (Site U1517). We draw the following main conclusions:

- Site GeoB20802: A chaotic and weakly reflective seismic unit (Unit H0) exists beneath the undeformed seafloor, in a depth interval from ~75-95 mbsf. Its chaotic seismic appearance, together with evidence for disruption of sediment laminations in core data, suggests that it is a

buried mass transport deposit. It was emplaced before the upper landslide of the Tuaheni Landslide Complex.

- Site GeoB20802: Pronounced undrained shear strength variations in sediment cores from Unit H0 correlate to bulk density fluctuations. The denser (and stronger) intervals correlate to sediments that are generally darker in colour and more laminated. Lighter, more homogenous intervals are typically less dense and weaker.

- A widespread reflector, termed the Intra-debris Reflector (Gross et al. 2018), can be traced into the intact sequence beneath the undeformed seafloor, where we refer to it as Reflector H1. The similar amplitude and phase of this reflection beneath both the undeformed seafloor and the upper landslide unit suggests that it has not been significantly altered by emplacement of the upper landslide. As such, we infer that the primary basal shear zone was distinctly above Reflector H1. Strength measurements at Site GeoB20802 indicate that there are three relatively weak intervals above Reflector H1 (between 67 and 88 mbsf). Any one of these weak intervals, or perhaps more than one of them, could have been exploited as a shear zone / shear zones.

- Site U1517: Drilling of landslide sediments in the Southern Lobe of the Tuaheni Landslide Complex provides insight into the origin of the Intra-debris Reflector (beneath the upper landslide unit, Unit II) and a deeper reflector termed the Base of Debris Reflector beneath the lower unit, Unit III. LWD data and physical property measurements demonstrate that the Base of Debris Reflector is the result of densification and velocity increase at the base of Unit III. The Intra-debris Reflector marks a subtle, local impedance drop, in the vicinity of the boundary between Units II and III. There is no significant shear strength reduction near the Intra-debris Reflector.

- Site U1517: An interval of low undrained shear strength near the base of the upper landslide unit in the Southern Lobe likely represents an induced weak layer that formed during landslide emplacement. This feature occurs distinctly above the Intra-debris Reflector (~10–15 m shallower), consistent with our interpretation from the Northern Lobe that the upper landslide unit was likely emplaced shallower than the Intra-debris Reflector.

- Free gas appears to be widespread in the sub-seafloor beneath the Tuaheni Landslide Complex, and there is evidence for gas accumulating directly beneath the upper landslide unit. This accumulation, at least in part, could be due to the effective sealing capacity of landslide deposits. Alternatively, it is possible that free gas played a significant role in pre-conditioning/triggering the slope to failure. Additional possible drivers are seismic shaking and associated transient fluid pressures.

- Methodologically, this study contributes to a recent impetus to combine high-resolution 3D P-Cable seismic data with logging data from MeBo200 and IODP drill holes (c.f. Riedel et al. 2020; Shankar et al. 2020). The integration of such datasets (that span the centimetre- to kilometre scale) enables the application of complementary geophysical methods, such as post-stack seismic inversions and rock physics investigations. The result is a step forward in our capability to predict sub-surface physical properties and tie them to geological processes.

7. Acknowledgements

8. References

Barnes, P.M., Pecher, I.A., LeVay, L.J., Bourlange, S.M., Brunet, M.M.Y., Cardona, S., Clennell, M.B., Cook, A.E., Crundwell, M.P., Dugan, B., Elger, J., Gamboa, D., Georgiopoulou, A., Greve, A., Han, S., Heeschen, K.U., Hu, G., Kim, G.Y., Kitajima, H., Koge, H., Li, X., Machado, K.S., McNamara, D.D., Moore, G.F., Mountjoy, J.J., Nole, M.A., Owari, S., Paganoni, M., Petronotis, K.E., Rose, P.S., Screaton, E.J., Shankar, U., Shepherd, C.L., Torres, M.E., Underwood, M.B., Wang, X., Woodhouse, A.D., and Wu, H.-Y., 2019. Site U1517. In Pecher, I.A., Barnes, P.M., LeVay, L.J., and the Expedition 372A Scientists, Creeping Gas Hydrate Slides. Proceedings of the International Ocean Discovery Program, 372A: College Station, TX (International Ocean Discovery Program). https://doi.org/10.14379/iodp.proc.372A.103.2019

Bloomer, S. F., & Mayer, L. A. 1997. Core-log-seismic integration as a framework for determining the basin-wide significance of regional reflectors in the eastern equatorial Pacific. Geophysical research letters, 24(3), 321-324. https://doi.org/10.1029/96GL02076

Böttner, C., Gross, F., Geersen, J., Crutchley, G.J., Mountjoy, J.J. and Krastel, S., 2018. Marine forearc extension in the Hikurangi margin: New insights from high-resolution 3-D seismic data. Tectonics, 37(5), pp.1472-1491. https://doi.org/10.1029/2017TC004906

Bünz, S., Mienert, J., and Berndt, C., 2003, Geological controls on the Storegga gas-hydrate system of the mid-Norwegian continental margin: Earth and Planetary Science Letters, v. 209, no. 3, p. 291-307. https://doi.org/10.1016/S0012-821X(03)00097-9

Cardona, S., Wood, L. J., Day-Stirrat, R. J., & Moscardelli, L. (2016). Fabric development and pore-throat reduction in a mass-transport deposit in the Jubilee Gas Field, Eastern Gulf of Mexico: consequences for the sealing capacity of MTDs. In Submarine Mass Movements and their Consequences (pp. 27-37). Springer, Cham. https://doi.org/10.1007/978-3-319-20979-1_3

Carey, J. M., Mountjoy, J. J., Crutchley, G. J., Lyndsell, B., and Petley, D. N., 2020, Laboratory Simulations of Submarine Landslide Failure Mechanisms. In Workshop on World Landslide Forum (pp. 173-178). Springer, Cham.

Conin, M., Bourlange, S., Henry, P., Boiselet, A., & Gaillot, P. (2014). Distribution of resistive and conductive structures in Nankai accretionary wedge reveals contrasting stress paths. Tectonophysics, 611, 181-191.

Cook, A.E., Sawyer, D.E., 2015, The mud-sand crossover on marine seismic data. Geophysics, 80(6), A109-A114. https://doi.org/10.1190/geo2015-0291.1

Couvin, B., Georgiopoulou, A., Mountjoy, J.J., Amy, L., Crutchley, G.J., Brunet, M., Cardona, S., Gross, F., Böttner, C., Krastel, S. and Pecher, I., 2020. A new depositional model for the Tuaheni Landslide Complex, Hikurangi Margin, New Zealand. Geological Society, London, Special Publications, 500(1), pp.551-566. https://doi.org/10.1144/SP500-2019-180

Crutchley, G. J., Geiger, S., Pecher, I. A., Gorman, A. R., Zhu, H., and Henrys, S. A., 2010, The potential influence of shallow gas and gas hydrates on sea floor erosion of Rock Garden, an uplifted ridge offshore of New Zealand: Geo-Marine Letters, v. 30, no. 3-4, p. 283-303. https://doi.org/10.1007/s00367-010-0186-y

DeMets, C., Gordon, R. G., and Argus, D. F., 2010, Geologically current plate motions: Geophysical Journal International, v. 181, no. 1, p. 1-80. https://doi.org/10.1111/j.1365-246X.2009.04491.x

Domenico, S.N., 1976. Effect of brine-gas mixture on velocity in an unconsolidated sand reservoir. Geophysics, 41(5), pp.882-894. https://doi.org/10.1190/1.1440670

Dugan, B. and Flemings, P.B., 2000. Overpressure and fluid flow in the New Jersey continental slope: Implications for slope failure and cold seeps. Science, 289(5477), pp.288-291. . https://doi.org/10.1126/science.289.5477.288

Elger, J., Berndt, C., Rüpke, L., Krastel, S., Gross, F., and Geissler, W. H., 2018, Submarine slope failures due to pipe structure formation: Nature communications, v. 9, no. 1, p. 1-6. https://doi.org/10.1038/s41467-018-03176-1

Field, M. E., and Barber, J. H. J., 1993, A submarine landslide associated with shallow seafloor gas and gas hydrates off Northern California, In: eds in Schwab, W. C., Lee, H. J., and Twichell, D. C., eds., Submarine Landslides: Selected Studies in the U.S. Exclusive Economic Zone, U.S. Geological Survey Bulletin 2002, p. 151-157.

Flemings, P. B., B. B. Stump, T. Finkbeiner, and M. Zoback (2002), Flow focusing in overpressured sandstones: Theory, observations, and applications, Am. J. Sci., 302(10), 827–855, doi:10.2475/ajs.302.10.827.

Flemings, P. B., Liu, X., and Winters, W. J., 2003, Critical pressure and multiphase flow in Blake Ridge gas hydrates. Geology, 31(12), 1057-1060.

Gross, F., Mountjoy, J. J., Crutchley, G. J., Böttner, C., Koch, S., Bialas, J., Pecher, I., Woelz, S., Dannowski, A., Micallef, A., Huhn, K., and Krastel, S., 2018, Free gas distribution and basal shear zone development in a subaqueous landslide – Insight from 3D seismic imaging of the Tuaheni Landslide Complex, New Zealand: Earth and Planetary Science Letters, v. 502, p. 231-243. https://doi.org/10.1016/j.epsl.2018.09.002

Hampton, M. A., Lee, H. J., and Locat, J., 1996, Submarine Landslides: Reviews of Geophysics, v. 34, no. 1, p. 33-59.

Hornbach, M. J., Saffer, D. M., and Holbrook, W. S., 2004, Critically pressured free-gas reservoirs below gas-hydrate provinces. Nature, 427(6970), 142-144.

François-Holden, C., Bannister, S., Beavan, J., Cousins, J., Field, B., McCaffrey, R., ... & Wallace, L. (2008). The Mw 6.6 Gisborne earthquake of 2007. Bulletin of the New Zealand Society for Earthquake Engineering, 41(4), 266-277.

Gibson, R. E. (1958), The progress of consolidation in a clay layer increasing in thickness with time, Geotechnique, 8, 171–182, doi:10.1680/geot.1958.8.4.171.

Higgs, B., Mountjoy, J. J., Crutchley, G. J., Townend, J., Ladroit, Y., Greinert, J., & McGovern, C. (2019). Seep-bubble characteristics and gas flow rates from a shallow-water, high-density seep field on the shelf-to-slope transition of the Hikurangi subduction margin. Marine Geology, 417, 105985.

Huhn, K. 2016. SO247 –SlamZ: Slide activity on the Hikurangi margin, New Zealand. RV Sonne Cruise Report. https://www.portal-forschungsschiffe.de/lw_resource/datapool/_items/item_157/so-247_wochenbericht_01.pdf

Kuhlmann, J., Orpin, A. R., Mountjoy, J. J., Crutchley, G. J., Henrys, S., Lunenburg, R., and Huhn, K., 2019, Seismic and lithofacies characterization of a gravity core transect down the submarine Tuaheni Landslide Complex, NE New Zealand: Geological Society, London, Special Publications, v. 477, no. 1, p. 479-495. https://doi.org/10.1144/SP477.37

Kvalstad, T.J., Andresen, L., Forsberg, C.F., Berg, K., Bryn, P. and Wangen, M., 2005a. The Storegga slide: evaluation of triggering sources and slide mechanics. In Ormen Lange–an Integrated Study for Safe Field Development in the Storegga Submarine Area (pp. 245-256). Elsevier. https://doi.org/10.1016/j.marpetgeo.2004.10.019

Kvalstad, T. J., Nadim, F., Kaynia, A. M., Mokkelbost, K. H., & Bryn, P., 2005b. Soil conditions and slope stability in the Ormen Lange area. Marine and Petroleum Geology, 22(1-2), 299-310.

L'Heureux, J.S., Longva, O., Steiner, A., Hansen, L., Vardy, M.E., Vanneste, M., Haflidason, H., Brendryen, J., Kvalstad, T.J., Forsberg, C.F. and Chand, S., 2011. Identification of weak layers and their role for the stability of slopes at Finneidfjord, northern Norway. In Submarine mass movements and their consequences (pp. 321-330). Springer, Dordrecht. https://doi.org/10.1007/978-94-007-2162-3_29

Lee, K., Yoo, D-G., McMechan, G.A., Hwang, N., Lee, G.H., 2013. A Two-Dimensional Post-Stack Seismic Inversion for Acoustic Impedance of Gas and Hydrate Bearing Deep-Water Sediments Within the Continental Slope of the Ulleung Basin, East Sea, Korea. Terr. Atmos. Ocean. Sci., Vol. 24, No. 3, 295-310. doi: 10.3319/TAO.2013.01.10.01(T)

Locat, A., Leroueil, S., Bernander, S., Demers, D., Jostad, H.P. and Ouehb, L., 2011. Progressive failures in eastern Canadian and Scandinavian sensitive clays. Canadian Geotechnical Journal, 48(11), pp.1696-1712. https://doi.org/10.1139/t11-059

Locat, J., Leroueil, S., Locat, A. and Lee, H., 2014. Weak layers: their definition and classification from a geotechnical perspective. In Submarine mass movements and their consequences (pp. 3-12). Springer, Cham. https://doi.org/10.1007/978-3-319-00972-8_1

Luo, M., Torres, M.E., Kasten, S. and Mountjoy, J.J., 2020. Constraining the age and evolution of the Tuaheni Landslide Complex, Hikurangi Margin, New Zealand using pore-water geochemistry and numerical modeling. Geophysical Research Letters, p.e2020GL087243. https://doi.org/10.1029/2020GL087243

Masson, D.G., Harbitz, C.B., Wynn, R.B., Pedersen, G. and Løvholt, F., 2006. Submarine landslides: processes, triggers and hazard prediction. Philosophical Transactions of the Royal Society A: Mathematical, Physical and Engineering Sciences, 364(1845), pp.2009-2039. https://doi.org/10.1098/rsta.2006.1810

Masson, D.G., Wynn, R.B. and Talling, P.J., 2010. Large landslides on passive continental margins: processes, hypotheses and outstanding questions. In Submarine mass movements and their consequences (pp. 153-165). Springer, Dordrecht. https://doi.org/10.1007/978-90-481-3071-9_13

Maurya, S.P. and Sarkar, P., 2016. Comparison of post-stack seismic inversion methods: a case study from Blackfoot Field, Canada. Int J Sci Eng Res, 7(8), pp.1091-1101.

Maurya S.P., Singh N.P., Singh K.H. (2020) Post-stack Seismic Inversion. In: Seismic Inversion Methods: A Practical Approach. Springer Geophysics. Springer, Cham. https://doi.org/10.1007/978-3-030-45662-7_3

McIver, R. D., 1977, Hydrates of natural gas--Important agent in geological processes: Geological Society of America Abstracts with Programs, v. 9, p. 1089-1090.

Micallef, A., Mountjoy, J. J., Krastel, S., Crutchley, G., & Koch, S. 2016. Shallow gas and the development of a weak layer in submarine spreading, Hikurangi margin (New Zealand). In Submarine Mass Movements and their Consequences (pp. 419-426). Springer, Cham.

Miramontes, E., Sultan, N., Garziglia, S., Jouet, G., Pelleter, E., Cattaneo, A. 2018. Altered volcanic deposits as basal failure surfaces of submarine landslides. Geology ; 46 (7): 663–666. doi: https://doi.org/10.1130/G40268.1

Mitchum, R. M., Sangree, J. B., Vail, P. R., & Wornardt, W. W. 1993. Recognizing sequences and systems tracts from well logs, seismic data, and biostratigraphy: Examples from the Late Cenozoic of the Gulf of Mexico: Chapter 7: Recent applications of siliciclastic sequence stratigraphy, 163-197. https://doi.org/10.1306/M58581C7

Moernaut, J., Wiemer, G., Kopf, A. and Strasser, M., 2020. Evaluating the sealing potential of young and thin mass-transport deposits: Lake Villarrica, Chile. Geological Society, London, Special Publications, 500(1), pp.129-146. https://doi.org/10.1144/SP500-2019-155

Mountjoy, J. J., McKean, J., Barnes, P. M., and Pettinga, J. R., 2009, Terrestrial-style slow-moving earthflow kinematics in a submarine landslide complex: Marine Geology, v. 267, no. 3–4, p. 114-127. https://doi.org/10.1016/j.margeo.2009.09.007

Mountjoy, J. J., Pecher, I., Henrys, S., Crutchley, G., Barnes, P. M., and Plaza-Faverola, A., 2014, Shallow methane hydrate system controls ongoing, downslope sediment transport in a low-velocity active submarine landslide complex, Hikurangi Margin, New Zealand: Geochemistry Geophysics Geosystems, v. 15, p. 4137-4156. https://doi.org/10.1002/2014GC005379

Paull, C. K., Buelow, W. J., III, W. U., and Borowski, W. S., 1996, Increased continental-margin slumping frequency during sea-level lowstands above gas hydrate–bearing sediments: Geology, v. 24, no. 2, p. 143-146. https://doi.org/10.1130/0091-7613(1996)024%3C0143:ICMSFD%3E2.3.CO;2

Pecher, I. A., Villinger, H., Kaul, N., Crutchley, G. J., Mountjoy, J. J., Huhn, K., ... & Coffin, R. B. 2017. A fluid pulse on the Hikurangi subduction margin: Evidence from a heat flux transect across the upper limit of gas hydrate stability. Geophysical Research Letters, 44(24), 12-385.

Pecher, I.A., Barnes, P.M., LeVay, L.J., Bourlange, S.M., Brunet, M.M.Y., Cardona, S., Clennell, M.B., Cook, A.E., Crundwell, M.P., Dugan, B., Elger, J., Gamboa, D., Georgiopoulou, A., Greve, A., Han, S., Heeschen, K.U., Hu, G., Kim, G.Y., Kitajima, H., Koge, H., Li, X., Machado, K.S., McNamara, D.D., Moore, G.F., Mountjoy, J.J., Nole, M.A., Owari, S., Paganoni, M., Petronotis, K.E., Rose, P.S., Screaton, E.J., Shankar, U., Shepherd, C.L., Torres, M.E., Underwood, M.B., Wang, X., Woodhouse, A.D., and Wu, H.-Y., 2019. Expedition 372A methods. In Pecher, I.A., Barnes, P.M., LeVay, L.J., and the Expedition 372A Scientists, Creeping Gas Hydrate Slides. Proceedings of the International Ocean Discovery Program, 372A: College Station, TX (International Ocean Discovery Program). https://doi.org/10.14379/iodp.proc.372A.102.2019

Piper, D.J., Cochonat, P. and Morrison, M.L., 1999. The sequence of events around the epicentre of the 1929 Grand Banks earthquake: initiation of debris flows and turbidity current inferred from sidescan sonar. Sedimentology, 46(1), pp.79-97. https://doi.org/10.1046/j.1365-3091.1999.00204.x

Reyners, M. 1998. Plate coupling and the hazard of large subduction thrust earthquakes at the Hikurangi subduction zone, New Zealand. New Zealand Journal of Geology and Geophysics, 41(4), 343-354.

Riedel, M., Freudenthal, T., Bergenthal, M., Haeckel, M., Wallmann, K., Spangenberg, E., Bialas, J. and Bohrmann, G., 2020. Physical properties and core-log seismic integration from drilling at the Danube deep-sea fan, Black Sea. Marine and Petroleum Geology, 114, p.104192. https://doi.org/10.1016/j.marpetgeo.2019.104192

Russell, B. and Hampson, D., 1991. Comparison of poststack seismic inversion methods. In SEG Technical Program Expanded Abstracts 1991 (pp. 876-878). Society of Exploration Geophysicists. https://doi.org/10.1190/1.1888870

Sawyer, D.E., Flemings, P.B., Dugan, B. and Germaine, J.T., 2009. Retrogressive failures recorded in mass transport deposits in the Ursa Basin, Northern Gulf of Mexico. Journal of Geophysical Research: Solid Earth, 114(B10). https://doi.org/10.1029/2008JB006159

Screaton, E.J., Torres, M.E., Dugan, B., Heeschen, K.U., Mountjoy, J.J., Ayres, C., Rose, P.S., Pecher, I.A., Barnes, P.M. and LeVay, L.J., 2019. Sedimentation controls on methane-hydrate dynamics across glacial/interglacial stages: An example from International Ocean Discovery Program Site U1517, Hikurangi Margin. Geochemistry, Geophysics, Geosystems, 20(11), pp.4906-4921. https://doi.org/10.1029/2019GC008603

Shankar, U., Ojha, M. and Ghosh, R., Assessment of gas hydrate reservoir from inverted seismic impedance and porosity in the northern Hikurangi margin, New Zealand. Marine and Petroleum Geology, 123, p.104751. https://doi.org/10.1016/j.marpetgeo.2020.104751

Stegmann, S., Strasser, M., Anselmetti, F., & Kopf, A. (2007). Geotechnical in situ characterization of subaquatic slopes: The role of pore pressure transients versus frictional strength in landslide initiation. Geophysical Research Letters, 34(7). https://doi.org/10.1029/2006GL029122

Stirling, M., McVerry, G., Gerstenberger, M., Litchfield, N., Van Dissen, R., Berryman, K., ... & Jacobs, K. 2012. National seismic hazard model for New Zealand: 2010 update. Bulletin of the Seismological Society of America, 102(4), 1514-1542.

Strasser, M., Moore, G.F., Kimura, G., Kopf, A.J., Underwood, M.B., Guo, J. and Screaton, E.J., 2011. Slumping and mass transport deposition in the Nankai fore arc: Evidence from IODP drilling and 3-D reflection seismic data. Geochemistry, Geophysics, Geosystems, 12(5). https://doi.org/10.1029/2010GC003431
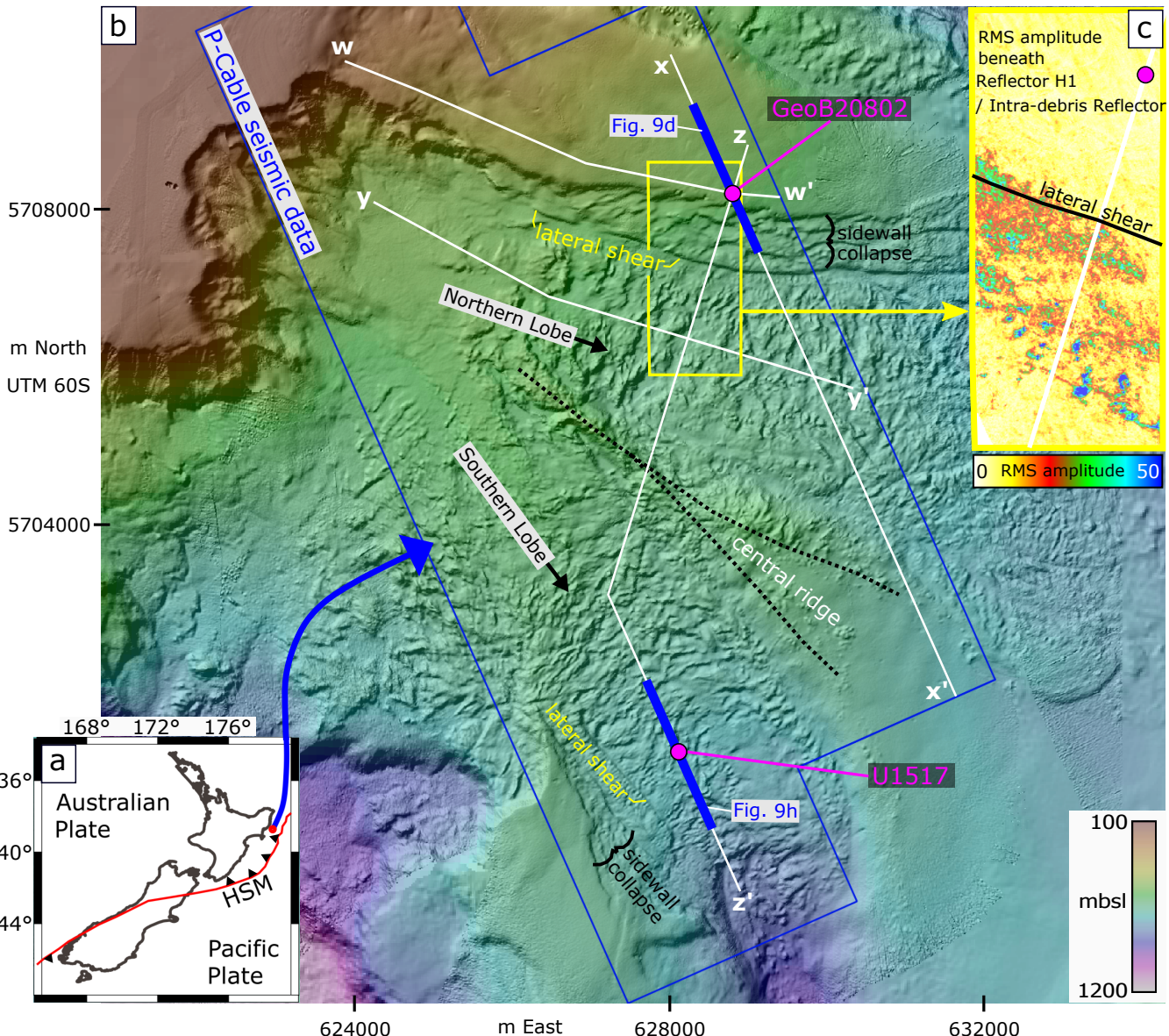
Sultan, N., Cochonat, P., Foucher, J. P., and Mienert, J., 2004, Effect of gas hydrates melting on seafloor slope instability: Marine Geology, v. 213, no. 1-4, p. 379-401. https://doi.org/10.1016/j.margeo.2004.10.015
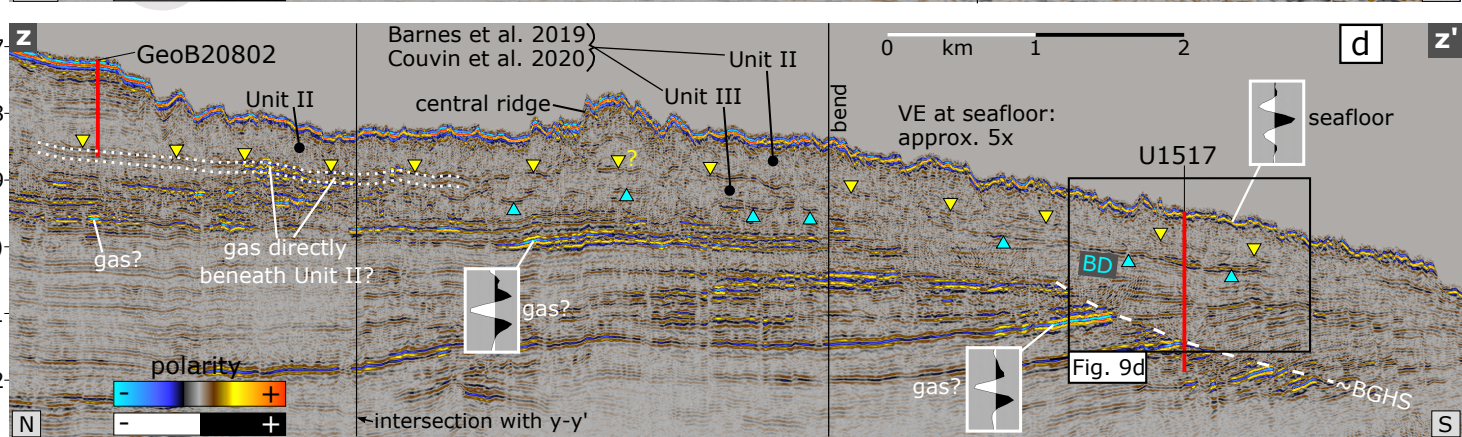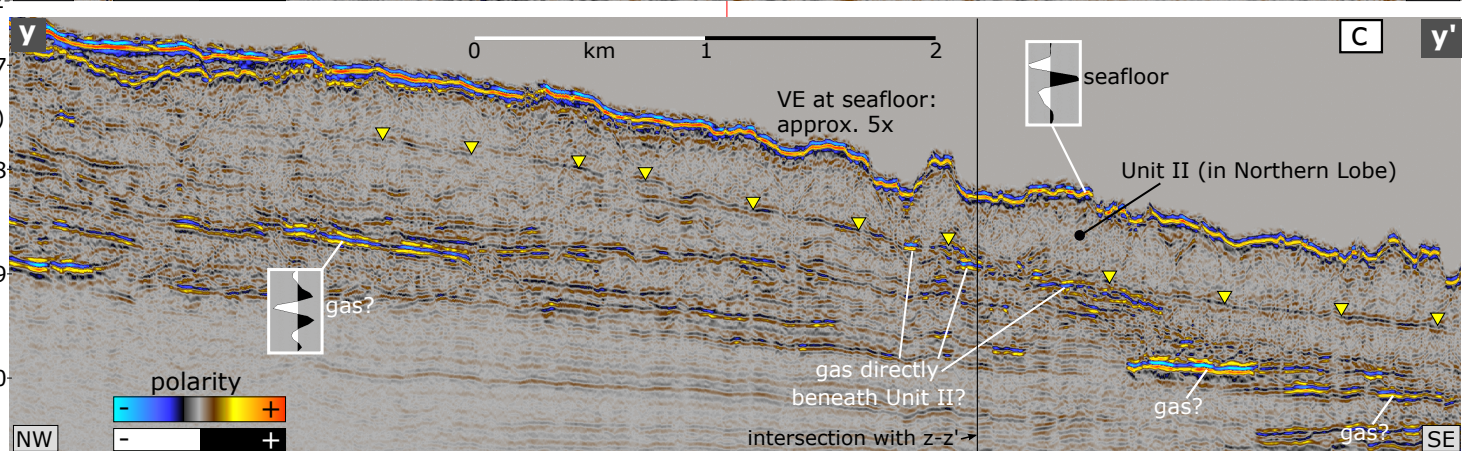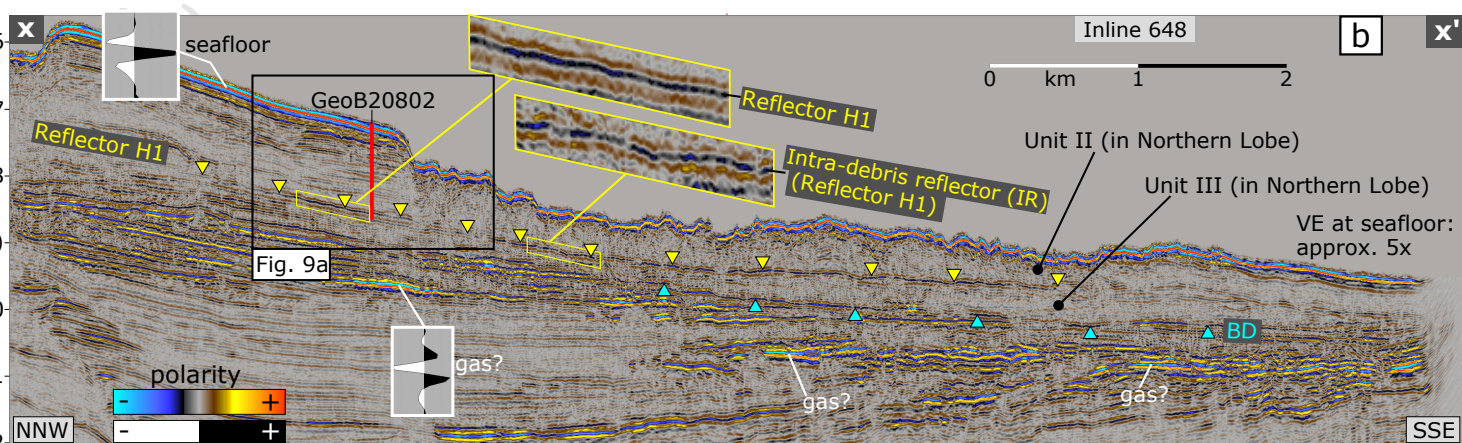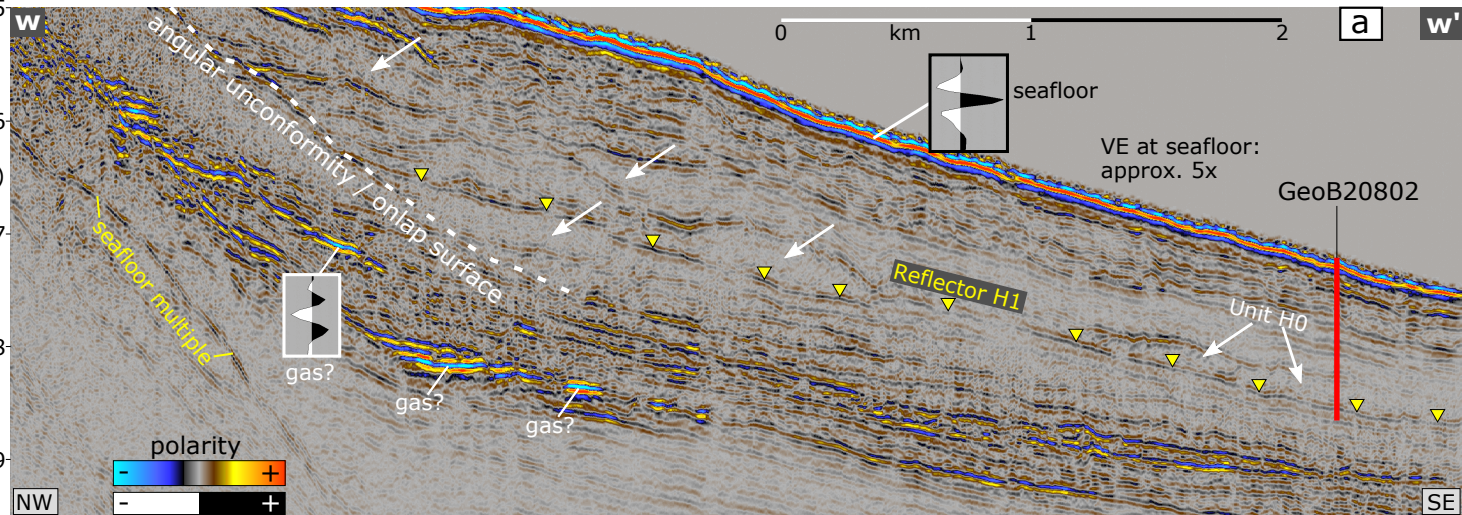
Sun, Q., Alves, T., Xie, X., He, J., Li, W. and Ni, X., 2017. Free gas accumulations in basal shear zones of mass-transport deposits (Pearl River Mouth Basin, South China Sea): An important geohazard on continental slope basins. Marine and Petroleum Geology, 81, pp.17-32. https://doi.org/10.1016/j.marpetgeo.2016.12.029
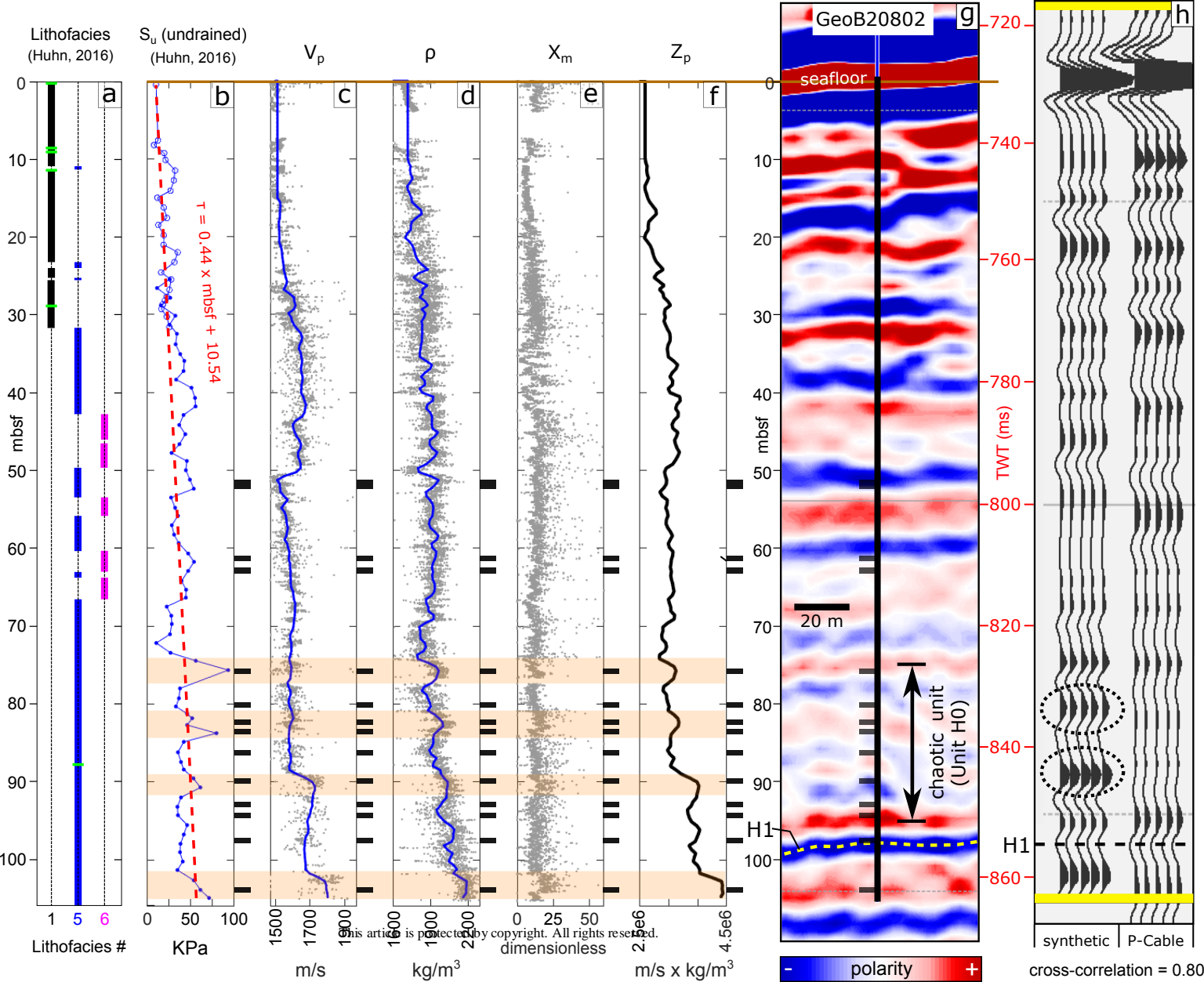
Talling, P., Clare, M., Urlaub, M., Pope, E., Hunt, J., and Watt, S., 2014, Large Submarine Landslides on Continental Slopes: Geohazards, Methane Release, and Climate Change: Oceanography, v. 27, no. 2, p. 32-45. https://doi.org/10.5670/oceanog.2014.38

Urlaub, M., Talling, P. J., and Masson, D. G., 2013, Timing and frequency of large submarine landslides: implications for understanding triggers and future geohazard: Quaternary Science Reviews, v. 72, no. 0, p. 63-82. https://doi.org/10.1016/j.quascirev.2013.04.020

Urlaub, M., Geersen, J., Krastel, S. and Schwenk, T., 2018. Diatom ooze: Crucial for the generation of submarine mega-slides? Geology, 46(4), pp.331-334. https://doi.org/10.1130/G39892.1

b

P-Cable seismic data

w

x

Fig. 9d

z

GeoB20802

w'

lateral shear

} sidewall collapse

Northern Lobe

y

y'

Southern Lobe

central ridge

lateral shear

x'

U1517

Fig. 9h

} sidewall collapse

z'

5708000

m North
UTM 60S

5704000

168° 172° 176°

a

Australian Plate

HSM

Pacific Plate

-36°

-40°

-44°

624000 m East 628000 632000

c

RMS amplitude beneath Reflector H1 / Intra-debris Reflector

lateral shear

0 RMS amplitude 50

100

mbsl

1200

Lithofacies (Huhn, 2016)

S_u (undrained) (Huhn, 2016)

V_p

ρ

X_m

Z_p

GeoB20802

seafloor

$\tau = 0.44 \times$ mbsf + 10.54

20 m

chaotic unit (Unit H0)

H1

mbsf

TWT (ms)

KPa

m/s

kg/m³

dimensionless

m/s x kg/m³

Lithofacies #

1 5 6

polarity

− +

synthetic | P-Cable

cross-correlation = 0.80

a — 11P-2 — dark greenish grey, clayey silt

b — 11P-3 — ← 2 cm thick, silt turbidite (core is darker and more laminated below this)

c — 14P-2A — ← color change, and a change to some irregular / contorted laminae

d — 14P-3A — irregular / contorted laminations continue

e — 18P-2A — shear strength peak ↗ greenish grey, clay-rich silt

f — 19P-3A — greenish grey, clay-rich silt

g — 20P-2 — alternatiing dark greenish grey and greenish grey, laminated clay-rich silt

a. 20P-3 — color lightens, dark color banding absent below

b. 21P-2 — greenish grey, clay-rich silt

c. 22P-2A — "fanning" laminae

d. 23P-2 — example core with widespread gas expansion (upon recovery)

e. 23P-3 — gas expansion features, as in (d); color change

f. 24P-3A — gas expansion features, as in (d); 3 cm thick, coarse silt, graded

g. 26P-2 — faintly-laminated, stiff, clay-rich silt; color change

Panel labels: a — Caliper (inches); b — Resistivity (Ωm); c — φ (dimensionless); d — V_p (m/s); e — ρ (kg/m³); f — Z_p (m/s x kg/m³); g; h — U1517; i

Depth axis: mbsf

Panel h: seafloor, IR, BD, 20 m, Iline 1776, Xline 4225

Panel i: TWT (ms), 950, 970, 990, 1010, 1030, IR, BD, synthetic, P-Cable, cross-correlation = 0.78

Lithological Legend
Barnes et al. 2019

silty clay / clayey silt

very fine sand - medium sand

alternating silt and clay layers

alternating sand / mud layers

a: 5f-1-a — thin sand interval — void (24.6–26.0 mbsf)

b: 6f-1-a — thick sandy intervals (29.3–30.8 mbsf)

c: 6f-2-a — thick sandy interval — void (30.8–32.1 mbsf)

d: 6f-3-a — thick sandy intervals (32.1–33.1 mbsf)

e: 6f-4-a (33.1–33.7 mbsf)

f: 7f-4-a — thick sandy interval — void — 7f-cc-a — 5820 — void (37.7–38.7 mbsf)

g: 8f-1-a — thick sandy interval (38.7–39.9 mbsf)

h: 8f-2-a — alternating silt and clay layers — silty clay / clayey silt — void (40.0–41.2 mbsf)

i: 8f-3-a — silty clay / clayey silt (41.4–42.4 mbsf)

(a) Normalized Amplitude vs Time (ms)

(b) Normalized Amplitude vs Frequency (Hz)

(c) GeoB20802 — Z_p (km/s × g/cm³), TWT (s), seafloor, Unit H0, H1

(d) P-Cable data — GeoB20802, 500 m, upper landslide deposit, Unit H0, H1, NW, SE

(e) Z_p inversion — GeoB20802, 500 m, upper landslide deposit, Unit H0, H1, (km/s)*(g/cm³), NW, SE

(f) GeoB20802 — P-Cable, Synthetic, Error, Unit H0, H1, Correlation = 0.93

(g) U1517A — Z_p (km/s × g/cm³), seafloor, BD, TWT (s), ~BGHS

(h) P-Cable data — upper landslide deposit, U1517A, IR, BD, gas, BGHS, 500 m, NW, SE

(i) Z_p inversion — U1517A, IR, BD, gas, BGHS, (km/s)*(g/cm³), 500 m, NW, SE

(j) U1517A — P-Cable, Synthetic, Error, IR, BD, BGHS, Correlation = 0.95

Reflector (R) / Lithostratigraphic Unit (LU)	Description
R: Seafloor	Seafloor reflector
LU: Unit I (Barnes et al. 2019; Couvin et al. 2020)	3 m thick Holocene drape sequence of greenish grey silty clay
LU: Unit II (Barnes et al. 2019; Couvin et al. 2020)	Upper landslide unit of the Tuaheni Landslide Complex. Responsible for the present-day seafloor morphology.
R: Intra-debris Reflector (Gross et al. 2018) Note: referred to as "R3" in Couvin et al. (2020)	Interpreted as the basal shear plane of the upper landslide unit (Unit II).
R: Reflector H1 (this study)	Equivalent to the Intra-debris Reflector, but also identified in this study within the intact (pre-failure) strata beneath the undeformed seafloor adjacent to the landslide.
LU: Unit H0 (this study)	Unit beneath the undeformed seafloor, directly above Reflector H1.
LU: Unit III (Barnes et al. 2019; Couvin et al. 2020)	Unit beneath the Intra-debris Reflector, interpreted as a submarine fan deposit.
R: Base of debris (Gross et al. 2018) Note: referred to as "R4" in the re-interpretation of Couvin et al. (2020)	Reflector marking the base of Unit III
R: BGHS (Mountjoy et al. 2014)	Seismic manifestations of the base of gas hydrate stability, including bottom simulating reflections (BSR)